Miguel Diogo Furtado Alexandre

Licenciado em Engenharia de Micro e Nanotecnologias

Theoretical Study of Optimum Luminescent Down-Shifting Properties for High Efficiency and Stable Perovskite Solar Cells

Dissertação para obtenção do Grau de Mestre em

Engenharia de Micro e Nanotecnologias

Orientador: Manuel J. Mendes, Post-Doc Fellow and Invited Assistant Professor,
Faculty of Sciences and Technology, NOVA University of Lisbon

Co-orientador: Rodrigo Martins, Full Professor,
Faculty of Sciences and Technology, NOVA University of Lisbon

Júri

Presidente: Dr. Hugo Manuel Brito Águas
Arguente: Dr. Maria Rute de Amorim e Sá Ferreira André
Vogal: Dr. Manuel João de Moura Dias Mendes

FACULDADE DE CIÊNCIAS E TECNOLOGIA
UNIVERSIDADE NOVA DE LISBOA

November, 2018

Theoretical Study of Optimum Luminescent Down-Shifting Properties for High Efficiency and Stable Perovskite Solar Cells

Este documento foi gerado utilizando o processador (pdf)LaTeX, com base no template "novathesis" [1] desenvolvido no Dep. Informática da FCT-NOVA [2].
[1] https://github.com/joaomlourenco/novathesis [2] http://www.di.fct.unl.pt

I would like to dedicate this work to my family.

Acknowledgements

Em primeiro lugar, gostaria de agradecer ao Professor Rodrigo Martins e à Professora Elvira Fortunato, por terem sido os fundadores deste magnífico curso onde estive nos últimos 5 anos, que me levou à descoberta de novas áreas, culminando no trabalho que aqui apresento.

Gostaria também de agradecer ao meu orientador, Professor Manuel Mendes, e co-orientador, Professor Rodrigo Martins, pela oportunidade de fazer uma tese na área dos fotovoltaicos, que é um tema de significante interesse para mim. Aos nomes anteriores, gostaria também de adicionar o Professor Hugo Águas e o Mestre Sirazul Zakir, pela ajuda e orientação que me deram durante este processo.

Não posso também deixar de fora todos os professores que, ao longo de todos os meus anos de ensino, me ajudaram a adquirir o conhecimento que hoje possuo, sendo que este trabalho não teria sido possível sem as suas contribuições.

Um obrigado muito especial para a minha família que sempre me suportou em todos os desafios que tive ao longo dos anos. Em especial, gostaria de mencionar o meu pai, a minha mãe e a minha irmã, que sempre foram as primeiras pessoas a ajudar-me a ultrapassar os problemas que tive, assim como, pelo seu esforço, também me permitiram que tivesse tido estes últimos 5 anos que significaram muito para mim.

Gostaria também de agradecer aos meus colegas Fábio Vieira e Manuel Chapa, com quem tive uma excelente semana para escrutinar teses, que ajudou a colmatar muitas das lacunas e bengalas que temos na escrita.

Por fim, mas não menos importante, gostaria também de agradecer aos meus amigos, com quem passei excelentes momentos ao longo destes últimos anos. Em especial, destaco os nomes João Teles, Manuel Chapa, Fábio Vieira, Débora Magalhães, João Pina, Ricardo Viana e Catarina Marques, Ana Pinheiro, Rita Fragoso e Maria Helena, sendo estas as pessoas com quem me dei mais.

Abstract

In recent years, the discovery of the excellent optical and electrical properties of perovskite materials made them one of focus of research in the area of photovoltaics, with its efficiency increasing significantly since its inception, in 2009. However, problems associated with the stability of these materials have hindered their widescale market application, with two examples being the UV degradation of the absorber material and the photoactivity, under 400 nm wavelengths, of TiO_2 which is one of the main materials used as an electron transport layer in these cells. Consequently, different methods were studied to minimize this degradation. One example consists in using down-shifting materials that change the harmful UV radiation to higher wavelengths that have no effect on the cell stability. Thus, this work is focused in the theoretical study of the photocurrent gains that can be attained by emulating the changed spectrum resulting from applying these materials, as well as the reduction in the harmful effects of UV radiation on perovskite solar cells. This first case analyzed resulted in gains of around 1% for planar cells and around 2% for cells with photonic structures. For the second optimized case, one was able to obtain a general reduction in generation in TiO_2 of one order of magnitude, coupled with a 80% reduction of perovskite's UV absorption.

Keywords: Photovoltaics, Photonic-enhanced Perovskite Solar Cells, Ultraviolet Stability, Down-shifting, Light Trapping

Resumo

A recente descoberta das excelentes propriedades óticas e elétricas das perovskites, para aplicações em células solares, fez com que se tornassem num dos principais alvos de estudo na área dos fotovoltaicos, levando ao rápido aumento da sua eficiência desde que foram introduzidas. Contudo, problemas associados com a estabilidade destes materiais tem limitado a sua implementação à larga escala. Alguns exemplos são a degradação do material fotoativo quando exposto a radiação UV, assim como a fotoatividade do TiO_2, para comprimentos de onda inferiores a 400 nm, uma vez que este se trata de um dos materiais mais usados como camada de transporte de eletrões nestas células. Consequentemente, diferentes métodos estão a ser estudados, de forma a minimizar esta degradação. Um exemplo, consiste em fazer *down-shifting* da radiação solar de forma a mudar a nefasta radiação UV para comprimentos de onda que não impactem a perovskite negativamente. Desta forma, este trabalho foca-se no estudo teórico dos ganhos de corrente gerada na célula devido à aplicação de *down-shifting*, em conjunto com os efeitos na nefasta geração no TiO_2. No primeiro caso, ganhos de cerca de 1% foram obtidos para células planares e cerca de 2% para células com estruturas fotónicas. Para o segundo caso otimizado obteve-se uma redução de uma ordem de grandeza na geração no TiO_2 e uma redução de 80% para a radiação UV absorvida pela perovskite.

Palavras-chave: Fotovoltaicos, Células Solares de Perovskite com Estruturas Fotónicas, Estabilidade à Radiação Ultravioleta, Down-shifting, Aprisionamento de Luz

Contents

List of Figures

List of Tables

Symbols

$E_{y_{i,j,k}}^{n+1/2}$ y-component of the electric field (V/m) located in grid i, j and k and time t.

$H_{y_{i,j,k}}^{n+1/2}$ y-component of the magnetic field intensity (A/m) located in grid i, j and k and time t.

μ Permeability of the medium (H/m).

$M_{x_{i,j,k}}$ Magnetic current density (V/m^2) located in grid i, j and k.

Δx x size for the Yee cell.

Δt Time step size.

v_{max} Maximum propagating velocity in the medium.

Abs Simulated absorption per unit volume (1/cm^3).

A Absorption resulting from the integration of the simulated absorption per unit volume.

ω Angular frequency (rad/s).

ϵ Relative permittivity.

J_{SC} Optical photocurrent value simulated (mA/cm^2).

G Generation rate per unit volume (1/cm^{3}s).

g Number of absorbed photons per unit volume (1/J cm^3).

$\hbar$ Reduced Planck constant ($1.054 \times 10^{-34} Js$).

$\Delta\lambda$ Shifting parameter used to emulate the Stokes shift present in down-shifting materials.

λ_C Absoprtion center for the hipothetical absorption profile used to simulate the effect of down-shifting.

n Refractive index.

$\boldsymbol{R_s}$ Specular reflection.

$\boldsymbol{R_d}$ Difuse reflection.

Acronyms

a-Si Amorphous silicon.

CIGS $CuIn_xGa_{1-x}Se_2$.

c-Si Crystalline silicon.

DS Down-shifted.

EA $CH_3CH_2NH_3^+$.

ETL Electron transport layer.

FA $NH_2CH{=}NH_2^+$.

FDTD Finite-difference time-domain.

HOIP Hybrid organic inorganic perovskite.

HTL Hole transport layer.

ITO Indium tin oxide.

LDS Luminescent down-shifting.

LSC Luminescent solar concentrators.

LTC Light trapping cell.

MA $CH_3NH_3^+$.

mp-TiO_2 Mesoporous TiO_2.

PBI Polymer background index.

PC Planar cell.

poly-Si Polycrystalline silicon.

PSC Perovskite solar cell.

PV Photovoltaic.

QD Quantum dots.

RE Rare earths.

Spiro 2,2',7,7'-tetrakis(N,N'-di-p-methoxyphenyl-amine)9,9'-spirobifluorene.

TCO Transparent conductive oxide.

UV Ultraviolet.

VBI Vacuum background index.

Motivation and Objectives

The ever-growing demand for clean energy has been one of the main proponents of research in the area of photovoltaics, with special focus on increasing the solar cells W/$ ratio to achieve a more competitive position in the market, when compared with other energy sources, such as fossil fuels and hydro-energy. The first steps taken to increase this ratio consisted in the optical and electrical optimization of the layers composing the solar cell. The former case relates to the trade-off between the solar cell thickness and the amount of material used in order to get best absorption using less materials, while the latter case is associated with the improvements in the electrical contact between the different solar cell layers as well as optimized material structure, leading to lower recombination. This way is then possible to get better solar cell performance, leading to an increase in the sunlight-to-electricity power conversion efficiency, coupled with lower material usage, i.e. lower g/W ratio.

In recent years, new research has started to emerge in the area of materials science centered in novel materials, such as perovskite and CIGS, with better electrical and optical properties, such as diffusion length and absorption coefficient - allowing for thin-film implementation of solar cells - when compared with the older, more conventional ones, such as silicon used in wafer-based photovoltaics. Thin-film technologies benefits from lower material usage, i.e. increased g/W ratio, when compared with wafer-based solar cells. Although these new materials have proven many times to come close or even surpass older materials conversion efficiencies, they still have many shortcomings that must be solved before they can be implemented into the market.

The need of overcoming these obstacles has been a big research driver in the field and has led to the work that will be presented in this thesis. By trying to emulate the effects of down-shifting in the solar spectrum, one will create a process that relates this mechanism with the solar cell absorption. Therefore, it will then be possible to optimize the relevant down-shifting parameters to get maximum photocurrent in the device as well as to test the effects of this process in the solar cell generation and UV absorption.

Work Strategy

The results obtained in this work were part of a three-step process:

1. The first step was the implementation of the code necessary to make the emulation of a shifted illumination spectrum. Afterwards, spectrums were obtained and compared with other similar results reported in the literature, to test the accuracy of the implemented method. Then, simulations were made to test if the change in spectrum would affect the simulation results in a predictable manner.

2. The next step consisted in designing the different perovskite solar cells in the simulation environment followed by extended validation to verify the accuracy of the simulation setup. Here, the base results, i.e. results with an unaltered spectrum, were also obtained

3. In the last step, the code implemented in the first point was used, together with the cells from the second point, with the objective of optimizing the relevant physical parameters of the DS mechanism in order to get maximum photocurrent density provided by the solar cell. These optimized parameters were then used to analyze the UV absorption of perovskite and the generation in TiO_2, allowing for a study of the effects of down-shifting in the device.

Chapter 1

Introduction

1.1 Solar Cell Market

Total global photovoltaic (PV) installed capacity increased over 600% from 2010 to 2016, going from under 50 GW to above 300 GW [1–3]. In 2015, the annual PV installed capacity was around 50 GW, matching the total global PV installed capacity until 2010 [1, 3, 4], illustrating the fast growth rate of this technology. One of the main reasons for this accelerated growth is the ever-increasing cost-competitiveness of solar power [3, 5]. To take an example, during the last 12 years, the material usage for crystalline and poly-crystalline solar cells (c-Si and poly-Si, respectively) decreased from around 16 g/Wp to 6 g/Wp [2]. These major improvements in material usage of silicon solar cells are one of the main reasons for its dominance in the market, leading to an increase in market share in the past years, going from around 80% to 90% [2, 5], while the remaining part is attributed to thin-film technologies. These emergent - thin-film - technologies aren't only based on silicon but use other materials like CdTe [5, 6], and $CuIn_xGa_{1-x}Se_2$ (CIGS) [5–9], that can achieve c/poly-Si conversion efficiencies while still maintaining a reduced thickness. Photovoltaics are still an area of active research, to keep increasing the cost-competitiveness of solar cells either by incremental improvements of current technologies or by investigating novel materials.

1.2 Perovskite Solar Cells

Materials based on the perovskite structure have received considerable attention from the photovoltaic comunity due to their exceptional optical and electrical properties, leading to a rapid increase in their conversion efficiency [10–15]. These reached a record efficiency higher than 22% in just a few years [16].

Perovskite compounds are based on an ABX_3 structure, where A and B represent cations of different sizes and X represents an anion [15, 17]. Figure 1.1 shows the unitary cell for perovskite, where the different circle colors and sizes represent the different ions and relative ion sizes, respectively. The most studied perovskites for solar cell applications are the hybrid organic inorganic perovskite (HOIP), where A is an organic or inorganic cation (methylammonium, $CH_3NH_3^+$; ethylammonium, $CH_3CH_2NH_3^+$; formamidinium, $NH_2CH{=}NH_2^+$, Cs and Rb), B is a divalent metal cation (Ge^{2+}, Sn^{2+}, Pb^{2+}) and X is a monovalent halogen anion (F^-, Cl^-, Br^-, I^-) [15, 17, 18]. In particular, the lead halide HOIPs have been one of the main perovskites studied due to their excellent optoelectronic properties [10, 11, 19–21].

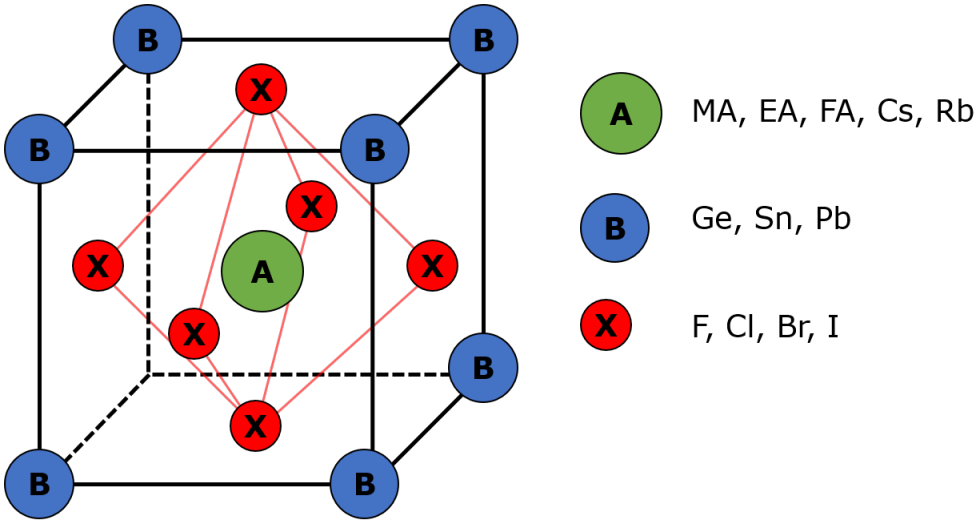

Figure 1.1: Unit cell for the basic ABX_3 perovskite structure. The circle sizes represent the different ion radius, meaning the A ion is the largest and the X ion the smallest. The colors refer to the different ions used. MA, EA and FA stand for methylammonium, ethylammonium and formamidinium, respectively.

Perovskite compounds show bandgap tunability by making composites of the various ions referred before [18, 22–24]. As an example, tuning the composition of the HOIP $MAPb(I_xBr_{1-x})$ allows for a bandgap variation from around 1.5 to 2.3 eV (with x = 1 and x = 0, respectively) [17, 21]. These bandgap variations can be combined with early theoretical studies for solar cell conversion efficiencies, to correlate the perovskite bandgap with the maximum conversion efficiency attainable. These studies use detailed balance arguments, where only radiative recombination is considered [25–27], to calculate the maximum theoretical conversion efficiencies as a function of the material bandgap for single junction pn cell [26], multiple junction cells [27, 28] and multiple junctions with solar concentration higher than unity [27–29].

Three typical architectures exist for Perovskite solar cells (PSCs) [15, 30, 31], as shown in Figure 1.2. The earliest configuration is based on mesoporous TiO_2 (mp-TiO_2) (Figure 1.2 a)). Here, the cell is made of transparent conductive oxide (TCO)/compact TiO_2/mp-TiO_2/perovskite absorber/hole transport layer (HTL)/metal contact layers. In the other 2,

the mesoporous layer is omitted and replaced by a compact electron transport layer (ETL). Both these cells only differ in the location of the HTL and ETL. In the n-i-p configuration the ETL is above the perovskite layer, while in the p-i-n configuration ETL changes place with the HTL. In the ETL, the most used material is TiO_2. However other materials, like ZnO and SnO_2, have also been studied [31]. On the other hand, the most relevant materials for the HTL are Spiro and PEDOT:PSS [31]. Recently, tandem applications have risen in popularity, where the HOIP is paired with CIGS [32] or silicon [33, 34].

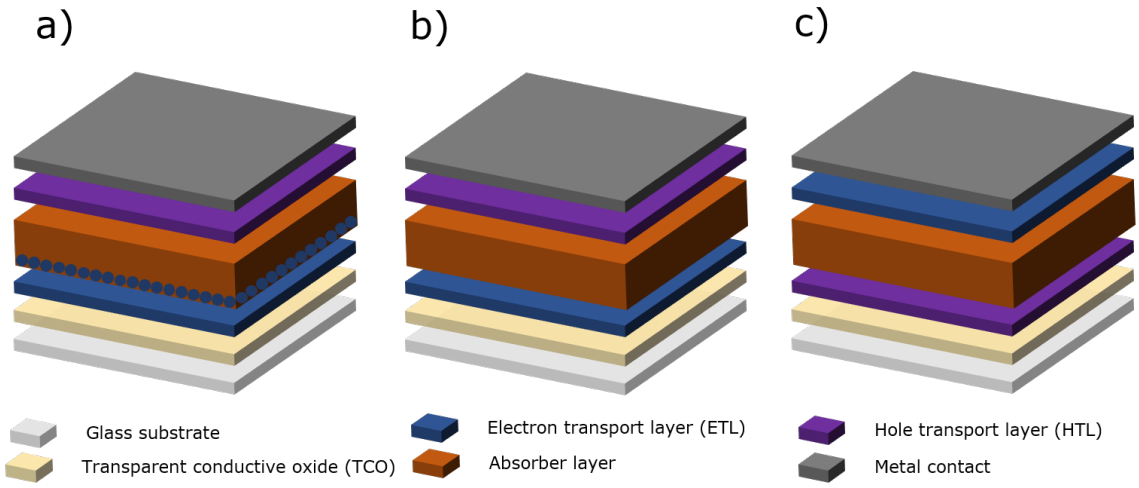

Figure 1.2: Schematic of the main PSCs architectures. a) cell with n-i-p configuration and mesoporous layer, b) cell with n-i-p configuration and c) cell with p-i-n configuration.

1.3 Luminescent Down-Shifting

Luminescent down-shifting (LDS) is the optical process of converting high energy photons into lower energy ones [35, 36]. The main LDS materials are dyes [37–39], quantum dots (QD) [40–43] and rare earth elements (RE) [44–46]. Initial research of these materials was mainly centered in the application to luminescent solar concentrators (LSCs), where the luminescent species would be added to a highly transparent plastic, which, by virtue of total internal reflection, could allow for inexpensive solar concentration spectrally matched with the solar cell [44, 45, 47–50]. In recent years, however, different type of applications, namely in PSCs, organic solar cells and dye sensitized solar cells have started to appear [51–54]. It has been shown that these cells suffer from stability problems associated with incident UV radiation [51, 55] and, for the first and latter cells, the presence of TiO_2, used as an ETL, due to the photocatalytic induced degradation of perovskite under 400 nm [56–59]. As a result, LDS materials have been applied to PSCs as a UV protection coating [52, 60–62]. This technology allows for the absorption of UV radiation, when compared with UV filters, that entirely block this radiation. These materials can also be applied to other types of solar cells, like CIGS and silicon, because of their small spectral response for lower wavelengths [36, 63].

1.4 Dielectric Photonic Structures

As stated earlier, the search for highly efficient solar cell technology at low costs is one of the main drivers for research, with many studies converging in technologies that allow smaller cell thickness - less material usage - without compromising optical performance. Some examples are the use of light trapping methods, such as metallic or dielectric nanoparticles on the rear side of the cell [64–66], texturing of the front or rear side of the cell [67–69] and the use of dielectric structures on top of solar cells [70–73], with the latter being the one used in this work. This method leads to the enhancement of the cell absorption due to 2 main reasons. Firstly, by forward scattering light, one can increase its travel path and, therefore, the likelihood of absorption. Secondly, one can also create resonant modes, related with the properties of the structures, that can significantly boost the absorption and, for periodic structures, even surpass the theoretical limit - the Tiedje-Yablonowitch limit - for specific wavelengths related with the structures' pitch [67, 74, 75].

1.5 Finite-Difference Time-Domain Simulation

The need for 3D simulation of solar cells with arbitrary geometries has led to the adoption of the finite-difference time-domain (FDTD) method, that was used in this work. As such, a brief description of the simulation methodology, based on references [76–78], will be presented next.

The FDTD method is based on an algorithm derived by Yee in 1966 [78], where the central difference approximation was applied to both space and time derivatives of Maxwell's curl equations to, with a discretization of space and time, create an iterative process to solve electromagnetic problems, such as the interaction between light and the solar cell, as used in this work.

The Yee algorithm is based on the Yee cell, shown in Figure 1.3, used to discretize the simulation space. Each cell has dimensions Δx, Δy and Δz and has its coordinates defined by the position in the simulation region. Similarly, time is also uniformly discretized as $t = n\Delta t$. As a result, one can express the field functions at any node within the discrete space. Using the discretization shown in Figure 1.3, it is then possible to approximate Faraday's equation via central differences, resulting in Equation 1.1 for the face shown in the right side of Figure 1.3, representing the approximation for the z component projection.

$$\mu\left(\frac{H^{n+1}_{z_{i-\frac{1}{2},j+\frac{1}{2},k}} - H^{n}_{z_{i-\frac{1}{2},j+\frac{1}{2},k}}}{\Delta t}\right) = \left(\frac{E^{n+\frac{1}{2}}_{x_{i-\frac{1}{2},j+1,k+1}} - E^{n+\frac{1}{2}}_{x_{i-\frac{1}{2},j,k+1}}}{\Delta y}\right) - \left(\frac{E^{n+\frac{1}{2}}_{y_{i-1,j+\frac{1}{2},k+1}} - E^{n+\frac{1}{2}}_{y_{i,j+\frac{1}{2},k+1}}}{\Delta x}\right) - M^{n+\frac{1}{2}}_{z_{i-\frac{1}{2},j+\frac{1}{2},k}} \tag{1.1}$$

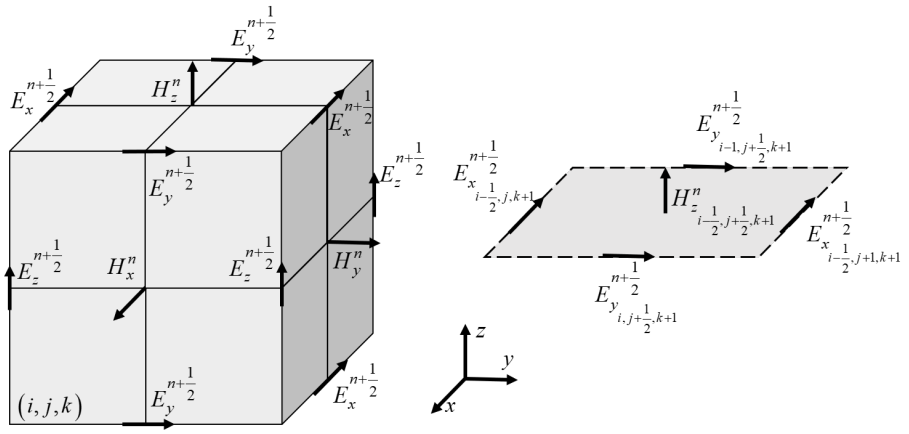

Figure 1.3: Schematic representation of the Yee algorithm. On the left is shown the Yee cell with the various corresponding fields. The direction of the fields in each face is chosen to satisfy Faraday's law. On the right, is shown the field with the full notation, including the spatial coordinates for the top face of the cube.

Using a similar procedure, it is also possible to obtain equivalent equations for the y and x-projections of Faraday's law (shown in Annex I). For the next step, one must create a secondary cell, where the electric and magnetic fields change position, allowing for a central difference approximation of Ampere's law, leading to equivalent equations to that of Equation 1.1. The equation for the x component of Ampere's law is also shown in Annex I, with the remaining components obtained in the similar manner to the ones from Faraday's law. Lastly, by combining the resulting equations from the last steps, one ends up with six equations that can be used, together with information of the field at an initial time, to create a recursive solution scheme to advance the fields through time. In Annex I these equations, used for the iterative process, are shown, assuming that $\boldsymbol{E_y^{n+1/2}}$, $\boldsymbol{E_z^{n+1/2}}$ and $\boldsymbol{H_x^n}$ are known. The Yee algorithm allows for the approximations used to be second order accurate, meaning the error decreases quadratically with decreasing size of the Yee cell, allowing for high accuracy results.

When applying this method, one always needs to satisfy the stability criterion, to avoid divergence of the fields during the calculation. This criterion relates the sizes of both time and space steps used as shown in Equation 1.2.

$$\Delta t < \frac{1}{v_{\max}} \frac{1}{\sqrt{\frac{1}{\Delta x^2} + \frac{1}{\Delta y^2} + \frac{1}{\Delta z^2}}} \tag{1.2}$$

The FDTD method is especially suited for this work, since it is a fast and simple method, that allows the simulation of arbitrarily shaped media, which is of particular importance when considering photonic structures, as well as inhomogeneous and lossy media. Lastly, it also allows for broadband frequency simulations, that reduce the simulation time required [67, 70, 76, 77]. In this work, a commercial-grade simulator based on this method was used [77].

Chapter 2

Simulation Setup

2.1 Solar Cell Structure

As stated in the previous chapter, this work uses the FDTD method, implemented in the commercial tool provided by Lumerical Solutions Inc. [77], to study the effects of LDS on the photo-generated current and generation profiles of PSCs. The schematic for the cells used in these simulations are shown in Figure 2.1 and the sizes summarized in Table 2.1. The various simulation parameters are described in Annex II. These cells are based on PSCs optimized to reach maximum photo-generated current. From Chapter 1, one can see that the materials used are some of the most common in the literature [31]. The relevant material properties are shown in Annex II.

This work is centered in 2 different cells. First, one will study planar cells, from now on referred to as PC, shown in Figure 2.1 a) and, secondly, a cell with TiO_2 hexagonally packed voids acting as light trapping structures, from now on called LTC, shown in Figure 2.1 b). The LTC uses TiO_2 since its properties, such as high dielectric constant and low absorption under 400 nm, make it a promising material for light trapping purposes [70]. For each architecture, 250 nm and 500 nm perovskite thicknesses were considered. The latter value represents a common optimized thickness for improved trade-off between opto-electrical performance and the solar cell degradation [15], while the second represents a common value when considering flexible applications [71, 79]. The LDS material is generally added to the cell by incorporating it into an encapsulation matrix [52, 60, 63] or by mixing it with the mp-TiO_2 used as ETL [54, 61]. For this purpose, only the first case is considered as it is the easier to simulate. The materials used as encapsulation are generally highly transparent polymers such as PMMA [52], EVA [63], PVB [63] and PS [60] with thicknesses in the order of micrometers. As a result, because the FDTD method is optimized for nanophotonic simulations, an approximation is used where the

air/encapsulation material reflection was neglected, since it wouldn't affect the main results in any meaningful way, and the background index of the simulation was changed to 1.5, which is a common value for these materials [80], case referred from now on as PBI - polymer background index. For the PC, a simulation with vacuum background index, from now on referred to as VBI, was still made as a reference.

Table 2.1: PC and LTC parameters. Ag, Spiro and ITO represent the respective material thicknesses. TiO_2, for the PC, represents the TiO_2 thickness and for the LTC is the TiO_2 thickness between perovskite and the structures beginning. t_{Voids} is the structures' TiO_2 thickness. R is the voids x and y radius, while R_z is the z radius. t_{Voids} is the distance between the center of 2 consecutive void structures, being given in function of R.

	Planar Cell (PC)		**Light Trapping Cell (LTC)**	
Perovskite thickness (nm)	250	500	250	500
R (nm)	-	-	401.2	388
R_z (nm)	-	-	1792	820.8
Pitch (×R)	-	-	2.2	2.3
ITO (nm)	50	76	63.6	62.3
TiO_2 (nm)	20	20	20	93.2
t_{Voids} (nm)	-	-	656.2	404.6
Spiro (nm)	150	150	150	150
Ag (nm)	80	80	80	80

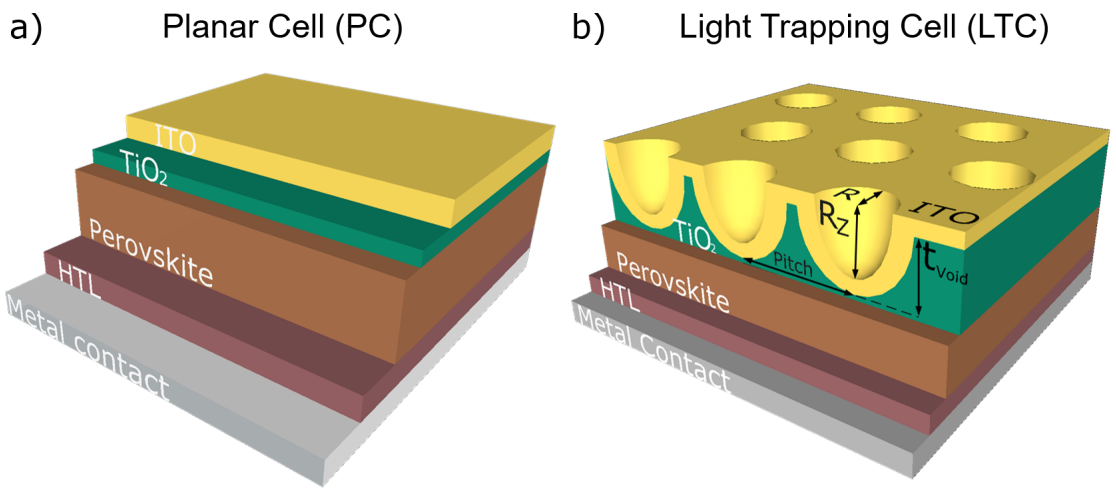

Figure 2.1: Schematic of the solar cells used in the simulations. a) Cell with planar structure, PC, used as reference and b) Cell with light trapping structures, LTC. The dimensions of the cell on the right refer to their respective counterparts in Table 2.1. The different layers properties are shown in Annex II.

Chapter 3

Results and Discussion

3.1 Optical simulation

The most important parameters for this work are the absorption, optical photocurrent, J_{ph} (mA/cm^2), and generation rate per unit volume, G (cm^{-3}s^{-1}). The second represents the maximum current obtainable by the cell, being also a figure of merit related with the cell's absorption. The latter represents the generated electrons per unit time through the entire volume. Considering the electromagnetic theory, one can relate these parameters with the fields resulting from the simulation and the respective material's properties [77]. The material's properties used in this work are provided by reference [80] and are also ploted in Annex II. Consequently, the absorption per unit volume, Abs (cm^{-3}), can be calculated using [77]:

$$Abs = -0.5\omega|E|^2 imag(\varepsilon) \tag{3.1}$$

Where ω is the angular frequency, ϵ is the material permittivity and $|E|^2$ is the square modulus of the electric field at the given point in the simulation region. By integrating the absorption per unit volume to calculate the cell absorption, A(ω), one can then use the solar spectrum to calculate J_{ph} by the following integral.

$$J_{ph} = \int A(\omega) AM_{1.5G} d\omega \tag{3.2}$$

Where $AM_{1.5G}$ represents the solar spectrum based on the ASTM G-173 global irradiance spectra [16]. This integral is of paramount importance, since the effect of the LDS layer is considered by changing the spectrum used in the integration, i.e. change $AM_{1.5G}$. The generation rate, G, is obtained by the integration of the number of photons per unit volume, g (J^{-1}cm^{-3}), over the simualtion spectrum. The latter is given by the following equation: $g = \frac{Abs}{\hbar\omega}$

3.2 Down Shifted Spectrum

The main objective of this work is to assess the optical effects of using LDS materials on PSCs by calculating J_{ph} and generation profiles when the cell is shined with a down-shifted (DS) spectrum. Consequently, the first step is to create a spectrum that would result from the interaction of the normal AM 1.5G spectrum with the LDS particles. Since this work does not focus on a particular type of LDS material, but instead, tries to study the general effect of DS, the setup used to create the shifted spectrum will be an ideal case that incorporates the main aspects of this process.

Based on emission and absorption profiles measured experimentally from various research groups for QDs [62, 81], dyes [38, 52, 82] and RE [44, 51], a gaussian profile was chosen to emulate those spectra as it is the closest shape to the experimental measurements. These gaussian profiles were considered to have unitary amplitude – this parameter will represent the percentage of photons that are absorbed – a dispersion of 50 nm and the gaussian center, λ_C, was left as an adjustable parameter for sweeps that will be shown in a later section. Following the choice of absorption and emission profiles, the AM1.5G spectrum photon flux, based on ASTM G-173, was employed, together with the gaussian profile, representing the absorption, to calculate the absorbed flux (blue plot in Figure 3.1 a)).

The absorbed flux was then shifted to create the emission flux (red plot in Figure 3.1). The value of this shift was left as a variable for future sweeps. Finally, to simulate the effect of DS, the AM1.5G spectrum was modified by adding the emission flux and subtracting the absorption flux. For simplicity, both absorption and emission plots were considered to be equal and no losses due to effects like isotropic emission of radiation, reabsorption and non-unitary photoluminescent quantum yield (PLQY) were considered.

Two examples of the resulting power profiles are shown in Figure 3.2. The plot on the left shows the AM 1.5G spectrum and 2 cases where λ_C was changed. For lower wavelengths a reduction of the overall power is observed, depending on the center of the gaussian profile used. It is also evident that there is a power increase in the region corresponding to λ_C plus the shift. On the right, the plot shows the effect of a change in the shifting parameter, $\Delta\lambda$, value. Where it can be seen that as $\Delta\lambda$ increases the peak is redshifted. The irradiance spectra obtained attend to the most important aspects resulting from the DS process, like lower power for lower wavelengths and analogously for higher wavelengths as observed by modelled results from Lesyuk et. al. [40, 41], also shown in Figure 3.1 b).

3.3 Planar Perovskite Solar Cells

Planar cells, introduced in Chapter 2, with different background indexes were first simulated. The index change represents the switch from the most common simulation environment – with vacuum background index, VBI – to a background with an index that

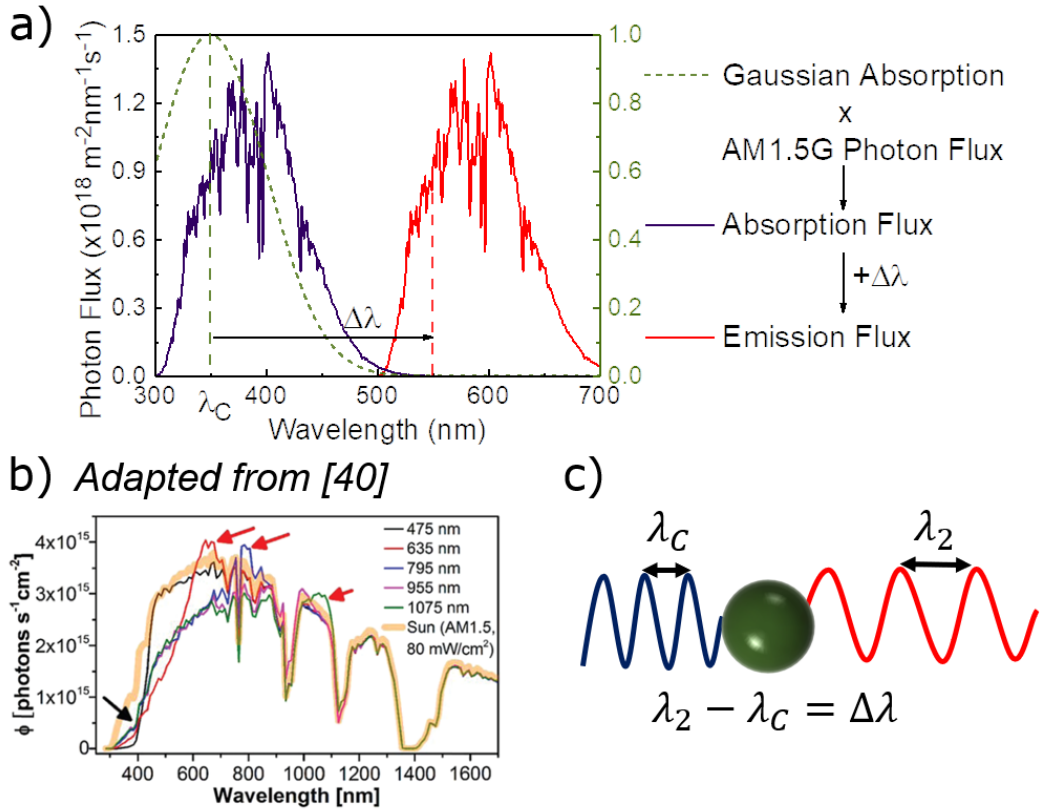

Figure 3.1: a) In solid line are the absorbed and emitted fluxes for λ_C of 350 nm and $\Delta\lambda$ of 200 nm. In dash line is the gaussian profile used to calculate the absorbed and emitted fluxes; b) Modelled spectra transmitted through a window prototype with varying QD properties and quantum yield of 50%. Adapted from reference [40]; c) Schematic of the DS process, where higher wavelength radiation is redshifted.

represents the presence of a matrix layer where the LDS particles can be embedded - polymer background index, PBI. In this second case, the reflection in the interface between the LDS material matrix and vacuum are not considered, given that these layers are generally several micrometers thick and, therefore the simulation methodology is not suited as it would require prohibitive amounts of computer memory. On the other hand, this reflection effect is ~4%, which is minimal and thus would not affect the main results in any significant way. These structures will also allow, due to the lack of photonic structures that lower the amount of UV absorbing materials, such as TiO_2 and ITO, to check the optical gains of the DS spectrum on a case where there is not a significant UV parasitic absorption.

3.3.1 Reflection Profiles

Initially, the total reflection and transmission profiles were calculated using the FDTD method, representing the numerical approximation to the theoretical results, and the transfer matrix method, obtained from the Fresnel equations for a 1D multistack, representing the analytical solution. By comparing both these results it is possible to verify the

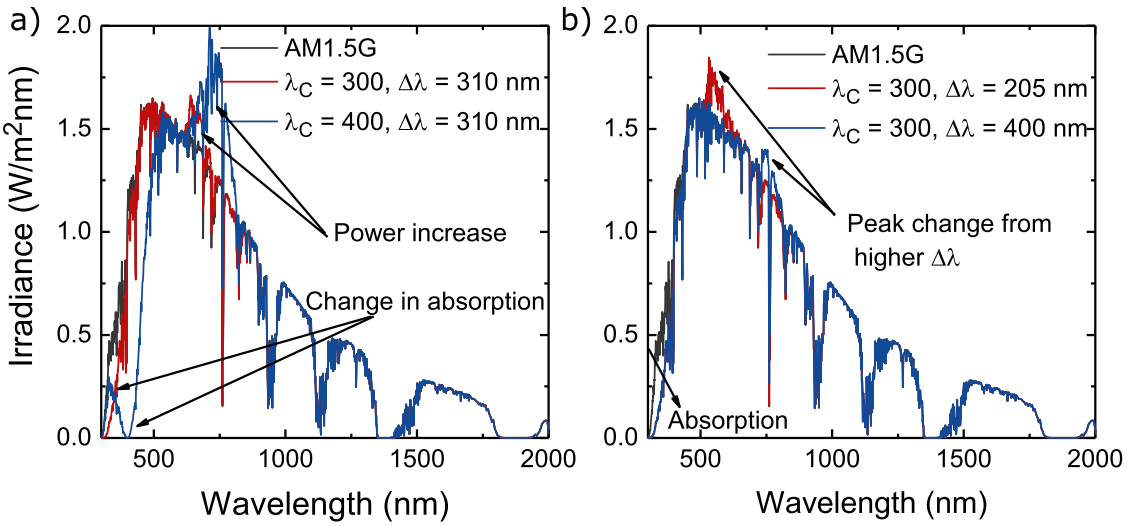

Figure 3.2: Resulting irradiance plots of the DS process used to simulate the effect of a LDS layer. a) AM1.5G spectrum, in black, and 2 examples of resulting spectrums when the $\Delta\lambda$ remains constant as 310 nm and λ_C changes from 300 nm to 400 nm, in red and blue, respectively, b) AM1.5G spectrum, in black, and 2 examples of the resulting spectrums when λ_C remains constant at 300 nm and $\Delta\lambda$ varies from 205 nm to 400 nm, in red and blue, respectively.

accuracy of these numerical results.

Reflection profiles have 2 main components, specular reflection, R_s, and difuse reflection, R_d. The method used for these results calculates the total reflection meaning both components are considered. However, because the results shown here are for PCs, there is no R_p, and thus the profiles for the PCs only have a specular component.

The reflection profiles for the 4 simulated PCs are shown in Figure 3.3. The equivalent transmission results are included in Annex III. From these plots, one can clearly see that the numerical simulation results make an excellent fit to theoretical curves over the entire simulation bandwidth. The inset profiles show the difference between the reflection values of the numerical simulation and theoretical results, validating the simulation method used as the difference is always inferior to 9×10^{-3}.

Considering the optical information shown in these graphs, one notices immediately the high reflection for wavelengths above 700 nm. When the cell thickness is increased, this effect is attenuated, as shown in Figure 3.3 b) and d) by the small dip around 900 nm. This effect results from Fabry Perot-like interference patterns arising from constructive interference of the propagating light [70]. However, the reflection, for the most part is still significative, reaching values up to 80%. Consequently, there is a need to create mechanisms to trap light and improve these losses, as will be further expanded later.

On the other side of the spectrum, under 700 nm, one can see the considerable low reflection, mainly attributed to the use of ITO as an anti-reflection coating. From Fresnel's equations it is known that smaller differences in material's refractive index, on an interface, leads to lower reflection. Considering ITO's index of 1.9, together with perovskite

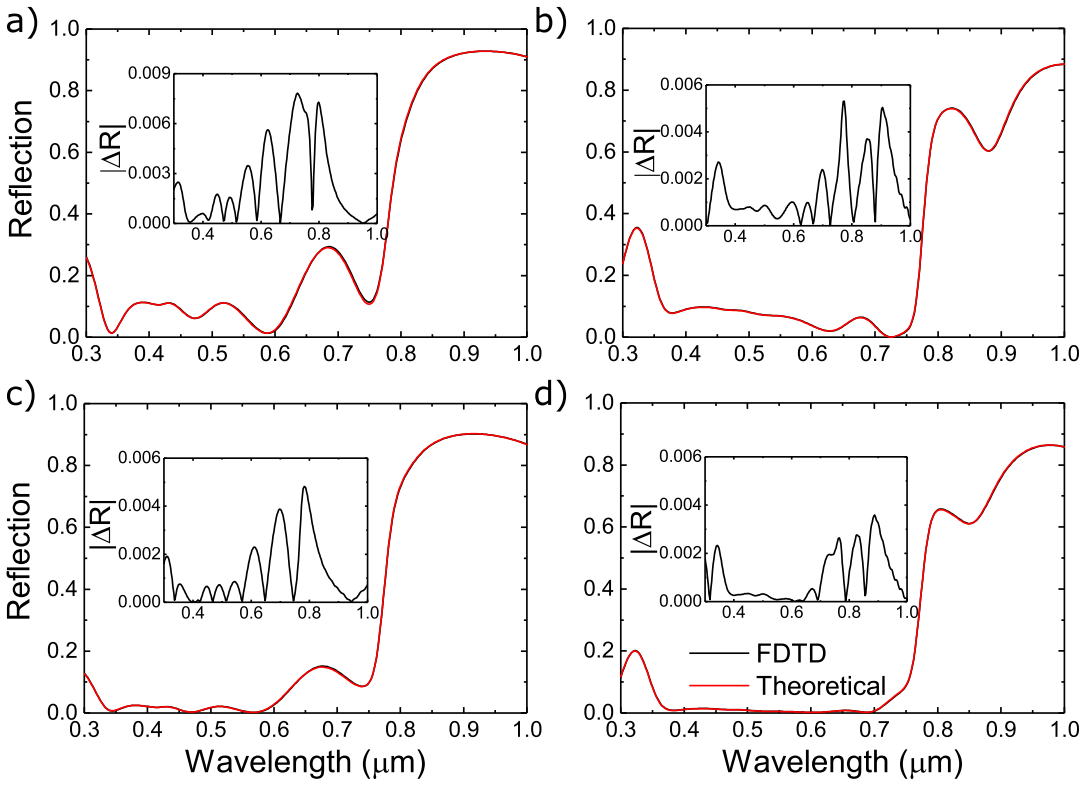

Figure 3.3: Reflection profiles with the results from the numerical simulation, in black, and the results from the theoretical simulation, in red. Inset is represented the modulus of the difference between the two methods. a) PC with 250 nm perovskite, b) PC with 500 nm perovskite, c) PC with background index of 1.5 and 250 nm perovskite, d) PC with background index of 1.5 and 500 nm perovskite.

or TiO_2's index of 2.5 (under 700 nm) [80], a lower reflection would indeed be expected, when compared with the vacuum index. This optical matching effect also explains the difference between the reflection under 700 nm for the VBI case (Figure 3.3 a) and b)) and the PBI case (Figure 3.3 c) and d)), since the latter provides a smaller index difference, when compared to ITO. In fact, due to the similar refractive index of the background and ITO, there are some points where the observed reflection is nearing 0% (ideal matching case).

3.3.2 Absorption Profiles

The absorption profiles were calculated as described in Section 3.1, by integrating the absorbed power per unit volume, and are displayed in Figure 3.4. These plots have 4 main components: the absorption due to the perovskite layer, curve in black; the TiO_2 layer, represented by the red shaded part; the remaining materials in the cell (ITO and Spiro), illustrated by the green shaded part. The last components are the inset profiles showing the absorbed power density throughout the cell for specific wavelengths, namely 350 and 900 nm. The first component is of paramount importance, as it represents the

absorption that will lead to the production of energy. The second component, due to TiO_2 being the main UV absorber in the cell, will also be very important to analyze the optical gains from the shifted spectrum. The third simply represents the general parasitic absorption. However, it should be noted that ITO also has parasitic absorption leading to photocurrent gains. The last component, the inset profiles, exhibit the absorption behavior for different wavelengths.

Because the transmition values, shown in Annex III, are negligeable, the absorption can be calculated from the reflection using $A = 1 - R$, where R is the reflection from the previous subsection, meaning that both these parameters are intimately related. For most of the simulation bandwidth the 500 nm cells – Figure 3.4 b) and d) – show higher absorption than its 250 nm counterpart – Figure 3.4 a) and c) – since in the former light will have a higher travel path. In the last subsection it was discussed that the PBI cells' reflection for wavelengths under 700 nm lowered around 10%, when compared with the VBI cells. This effect is also enhanced in these plots where the cell has better index matching. Also present in these graphs is the lower absorption for wavelengths above 800 nm, that will be further analyzed in a later section, when the LTCs are introduced.

A relevant aspect present is the TiO_2's parasitic UV absorption - reaching values between 10-20% under 400 nm - where the TiO_2 is optically active. Despite the TiO_2 reduced thickness, these values are still significant and impact perovskite's absorption in these wavelengths. As will be shown in a later section, the increase in TiO_2 thickness will lead to a further decrease in perovskite absorption due to higher absorption of this material, completely blocking the UV radiation from reaching the absorber.

For the remaining materials, in the most energetic section of the spectrum, the absorption is mainly attributed to the ITO layer, as it is the first one in the cell, reaching values up to 20%. These absorption figures are corroborated by the inset profiles with the absorbed power for 350 nm, where it can be seen that Spiro's absorption is almost negligible, being ITO and TiO_2 the second higher absorbers, after perovskite. Consequently, it is expected that, with the use of a LDS material to change the incident spectrum, one will be able to mitigate the unwanted electron generation in these layers, shifting the photo-generation to the absorber layer.

For higher wavelength photons, there is parasitic absorption from both Spiro and ITO. From the inset profiles on the right, that show the absorbed power for 900 nm, one can see that these materials can reach similar absorption values to those of perovskite. Although this study is not the main focus of this work, it is also important to note that by reducing these parasitic absorptions and, therefore, increasing perovskite's absorption, one can increase the cell's J_{ph}, as shown in recent works by Mendes et.al. [70, 71]. From the standard AM 1.5G spectrum, shown in Section 3.2, it can be seen that there is still some relevant radiation for wavelengths above 800 nm.

Considering the absorption values above 80% for wavelengths ranging from 400 to 750 nm, the excellent absorption properties of perovskite are seen. Several equivalent studies, for amorphous silicon (a-Si) solar cells [70, 74], crystalline silicon cells [70], CIGS

cells [64] and even GaAs cells [68], show lower absorption for an equivalent wavelength range, when compared with perovskite's. These outstanding absorption properties make perovskite a very compelling material for solar cells and this is, to some extent, part of the reason they are so widely studied.

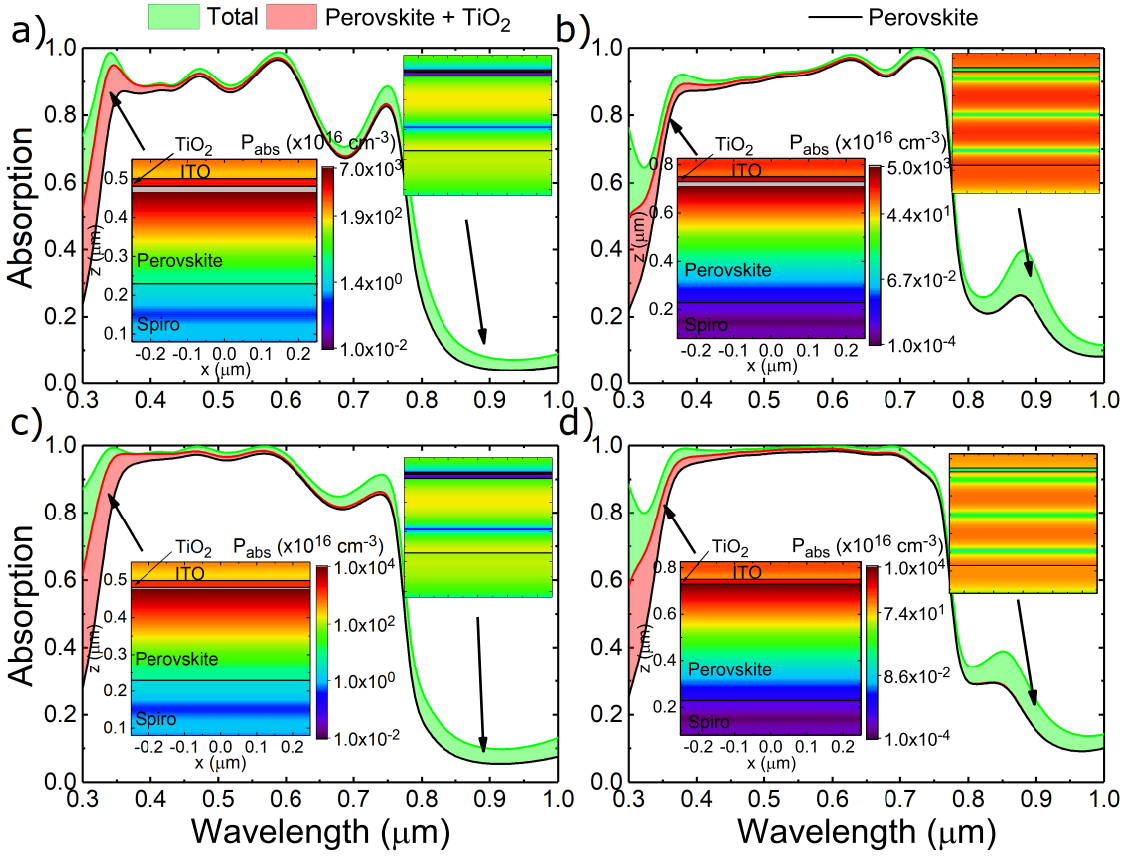

Figure 3.4: Absorption profiles with the absorption on the perovskite layer, in black; the TiO_2 layer, in red; and the total cell absorption, in green. The inset profiles show the plots for the absorbed power density through the cell volume for specific wavelengths, indicated by the arrows. The leftmost graph is the absorbed power for 350 nm and the rightmost graph is the absorbed power for 900 nm. a) and b) PC with VBI for 250 nm and 500 nm perovskite, respectively; c) and d) PC with PBI for 250 nm and 500 nm perovskite, respectively.

3.3.3 Photocurrent Shifts

Together with the solar spectrum, the calculated absorption profiles, can be employed to obtain the maximum value of photocurrent in the cell, as described in Section 3.1. These values act as a figure of merit of the optical performance of the cell and, therefore can be used to compare different cell architectures.

By integrating different spectrums, using the process shown earlier in Figure 3.1, one can emulate the effect on J_{ph} of having an LDS material on top of the cell. Consequently, a sweep was made, where λ_C was varied between 300 and 400 nm and $\Delta\lambda$ between 100

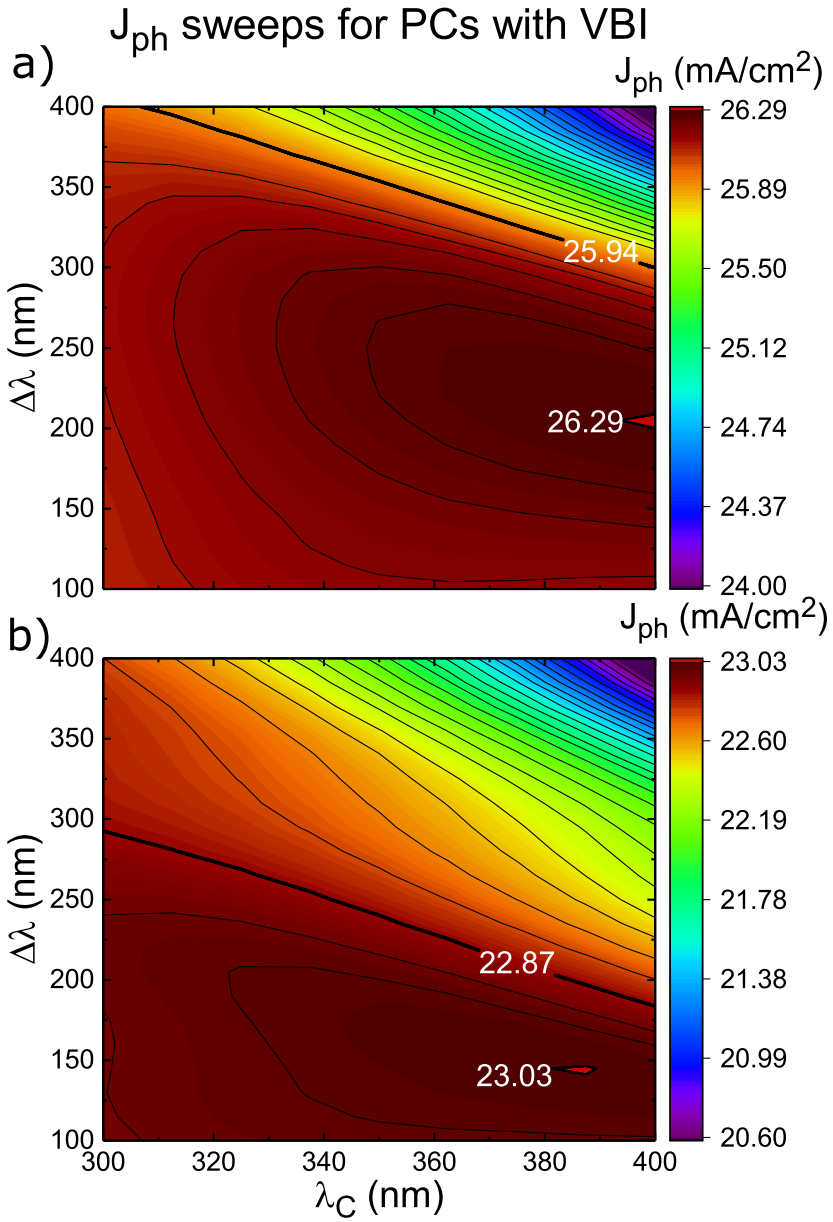

Figure 3.5: Contour plots for the sweeps where λ_C and $\Delta\lambda$ were varied from 300 nm to 400 nm and 100 nm to 400 nm, respectively. a) PC with VBI for 500 nm perovskite layer and b) PC with VBI for 250 nm perovskite layer. The thicker line represents the contour corresponding to the photocurrent value obtained for the pristine spectrum. The indicated values represent the respective contour photocurrent value. The topmost value refers to the contour representing the pristine value, while the bottommost refers to the highest value contour in the plot.

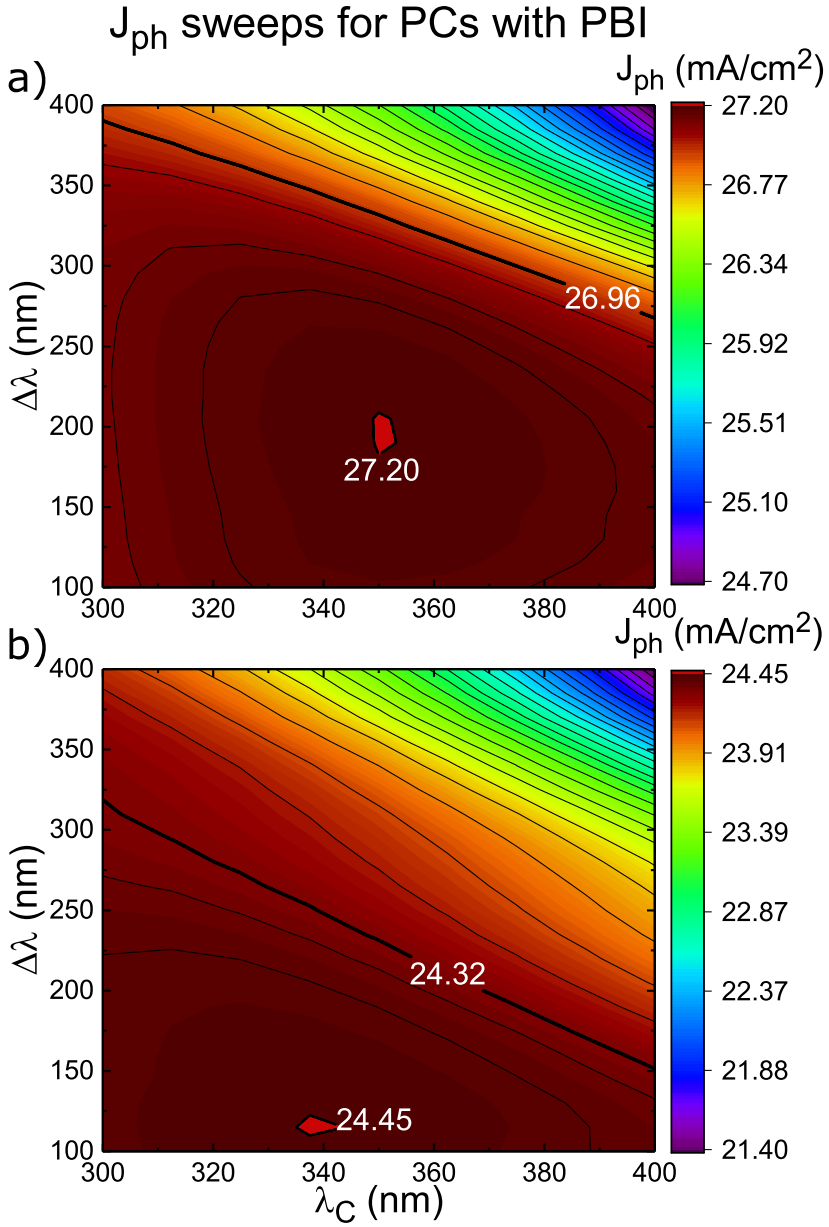

Figure 3.6: Contour plots for the sweeps where λ_C and $\Delta\lambda$ were varied from 300 nm to 400 nm and 100 nm to 400 nm, respectively. a) PC with PBI for 500 nm perovskite layer, b) PC with PBI for 250 nm perovskite. The thicker line represents the contour corresponding to the photocurrent value obtained for the pristine spectrum. The indicated values represent the respective contour photocurrent value. The topmost value refers to the contour representing the pristine value, while the bottommost refers to the highest value contour in the plot.

and 400 nm. The resulting plots are shown in Figure 3.5 for the VBI cell and in Figure 3.6 for PBI cell.

In all cases, the trend when both parameters change is similar and give a general idea of how the changing spectrum can influence the maximum current output. When considering $\Delta\lambda$ above 250 nm, J_{ph} drops steadily to a minimum, reaching values 2 mA/cm^2 lower than the pristine value, shown by the thicker line in the different plots. The absorption profiles from the last section show that, above 800 nm there is a significant reduction in the cell absorption, associated with the perovskite bandgap, ~1.55 eV, used for these simulations. Consequently, when the $\Delta\lambda$ is significantly increased, the spectrum gets redshifted, Figure 3.1, to where the cell has lower performance negatively impacting its optical response.

In Table 3.1 the J_{ph} for the pristine and optimized spectrums are summarized, together with their absolute and relative differences. Here it is seen that the differences are small, with a maximum of 0.35 mA/cm^2(1.3%) for the VBI cell with 500 nm perovskite. The thin TiO_2 layer used in these cells is the main factor inhibiting this increase as it is the main UV absorber before perovskite. This lower parasitic absorption is optically advantageous, as it allows for an increase in perovskite's absorption. However, practically, it has some issues related with the UV degradation of $MAPbI_3$. Several reports have studied the degradation mechanisms, but the full picture hasn't yet been totally understood. Nonetheless, one of the points of focus has been the creation of I_2 that leads to the structural decomposition of perovskite's crystal [55, 57]. This can appear at the TiO_2/perovskite interface from TiO_2's catalytic effects [57] and from the known photolysis of PbI_2 present in the perovskite's structure [55]. Therefore, on one side, the UV shading of the cell produced by a thicker layer of TiO_2 could be seen as beneficial, reducing this degradation in detriment of the photocurrent that would be generated otherwise. However, considering TiO_2's photocatalytic effects under 400 nm the use of either a UV filter or LDS are preferred to avoid perovskite's degradation, with the latter enabling the reabsorption of the otherwise lost radiation [52].

The optimized $\Delta\lambda$ and λ_C values for the J_{ph} from Table 3.1 are summarized in Table 3.2. Adding these values, the result varies between 400 to 500 nm, representing the wavelengths to where the spectrum is shifted. Given that these values depend heavily on the device absorption, which is more prevalent in the 400-700 nm range (Figure 3.4), these results were expected.

3.3.4 Generation Profiles and UV absorption

The generation profiles were calculated, as explained in Section 3.1, for the pristine spectrum and the one corresponding to the optimized $\Delta\lambda$ and λ_C values, shown in Section 3.3.3. The results for the PCs with VBI are shown in Figure 3.7 and, for the cells with PBI, in Figure 3.8. For all cases in study, the main difference is the reduction of the harmful photo-generation in the TiO_2 layer. This value varied from around $2 \times 10^{26} cm^{-3} s^{-1}$ to

Table 3.1: Summary of the optimized results obtained for the different PCs simulated. AM1.5G J_{ph} represents the values obtained in the pristine case and Shifted J_{ph} represents the optimized values resulting from the sweeps for each individual case. It is also shown the absolute and relative difference between the two.

Background refractive index	1		1.5	
Perovskite thickness (nm)	250	500	250	500
AM1.5G J_{ph} (mA/cm^2)	22.87	25.94	24.32	26.96
Shifted J_{ph} (mA/cm^2)	23.03	26.29	24.45	27.20
ΔJ_{ph} (mA/cm^2)	0.16	0.35	0.13	0.24
ΔJ_{ph} (%)	0.7	1.3	0.5	0.9

Table 3.2: $\Delta\lambda$ and λ_C values corresponding to the optimized values of J_{ph} obtained from the sweeps.

Background refractive index	**Perovskite thickness (nm)**	**λ_C(nm)**	**$\Delta\lambda$(nm)**
1	250	387.5	145
	500	400.0	205
1.5	250	337.5	115
	500	350.0	205

$1\times10^{26}cm^{-3}s^{-1}$ for both 250 and 500 nm cells with VBI, and from around $3\times10^{26}cm^{-3}s^{-1}$ to $0.2\times10^{26}cm^{-3}s^{-1}$ for the PBI case. Thus, the photo-generation changes to 50% and 7% of the original value, deriving from the lower UV radiation irradiated onto the cell.

As a result of the TiO_2's reduced absorption, an increase in the perovskite's photo-generation is observed as indicated in Figure 3.7 and 3.8. Equivalently, an increase in Spiro's parasitic absorption was also obtained. One can attribute this latter addition to the increase in higher wavelength radiation, which has a higher penetration depth on the cell.

Perovskite's UV absorption was considered by calculating J_{ph} for wavelengths between 300 nm and 400 nm, because, as was explained earlier, this parameter is intimately related with the solar cell's absorption. For the PC with 250 nm and VBI, these values were 1.00 mA/cm^2, with the pristine spectrum, and 0.15 mA/cm^2, with the optimized spectrum. In the 500 nm perovskite layer case, the same values were 1.00 mA/cm^2 and 0.20 mA/cm^2. Considering now the PBI cases, one obtained for the 250 nm cell 1.17 mA/cm^2 and 0.27 mA/cm^2 for the optimized and pristine spectrums, respectively, and, for the 500 nm cell, 1.09 mA/cm^2 and 0.16 mA/cm^2. The corresponding percentual differences range from 75-85%, suggesting a significant reduction in the material UV absorption.

From these results, it can be inferred that either the TiO_2's photoactivity and perovskite's degradation under UV radiation would be reduced, even when one takes into account the non-ideal DS effects here suppressed, allowing these cells to maintain their

performance figures for a longer time period. Later, this point will be further expanded for the LTC. It can also be added that a small reduction in the ITO layer photo-generation was also achieved.

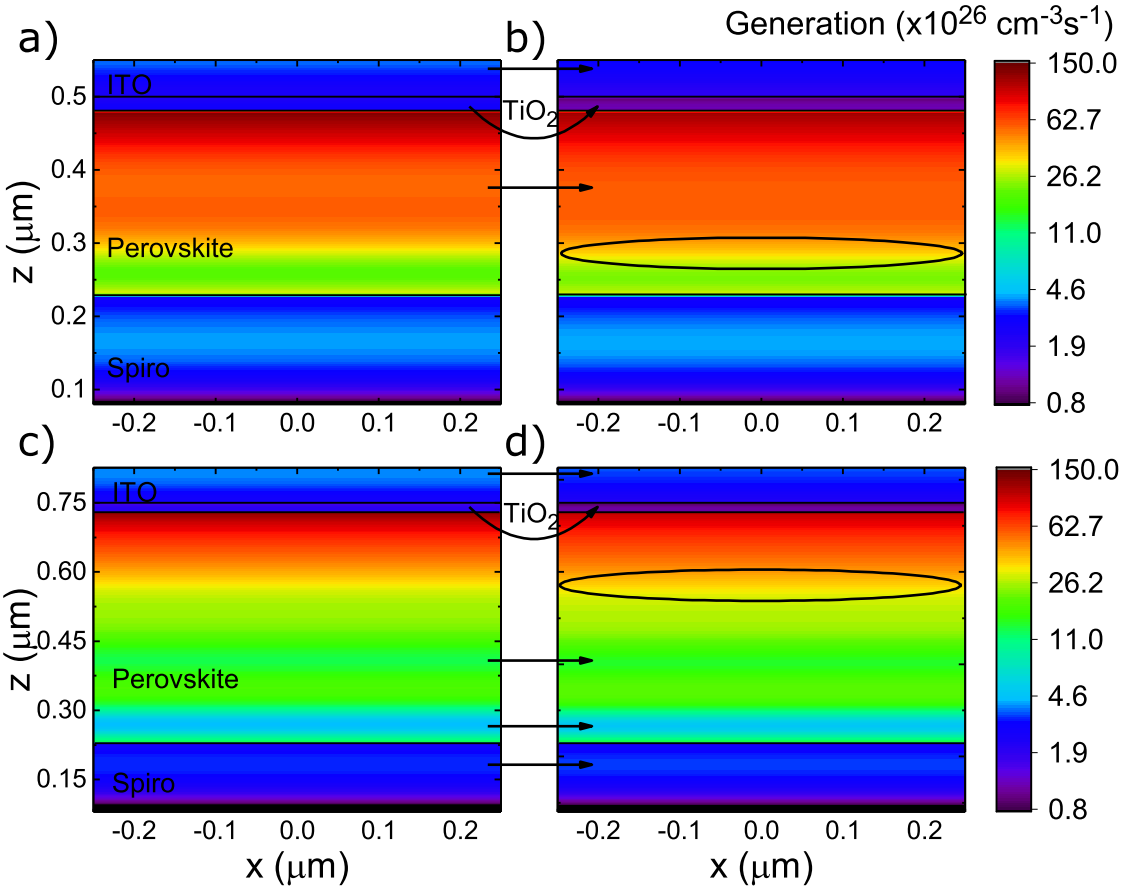

Figure 3.7: Generation profiles for the PCs with VBI. a) cell with 250 nm perovskite; b) cell with 250 nm perovskite and optimized spectrum; c) cell with 500 nm perovskite; d) cell with 500 nm perovskite and optimized spectrum. The arrows and ellipse mark the biggest changes in the plots.

3.4 Solar Cells with Dielectric Photonic Structures

In this section, the focus is in the cells with photonic structures. As stated earlier, PC performance suffers from significant losses associated with lower absorption for higher wavelengths, paving the way for the development of different methods to mitigate these losses.

In this work, high dielectric constant structures are considered for use on top of solar cells to act as forward scatterers of light, causing an increase of its travel path, and, consequently, their chance of being absorbed [72, 74]. The use of these structures can also lead to the creation of localized modes in the absorber material that will then increase

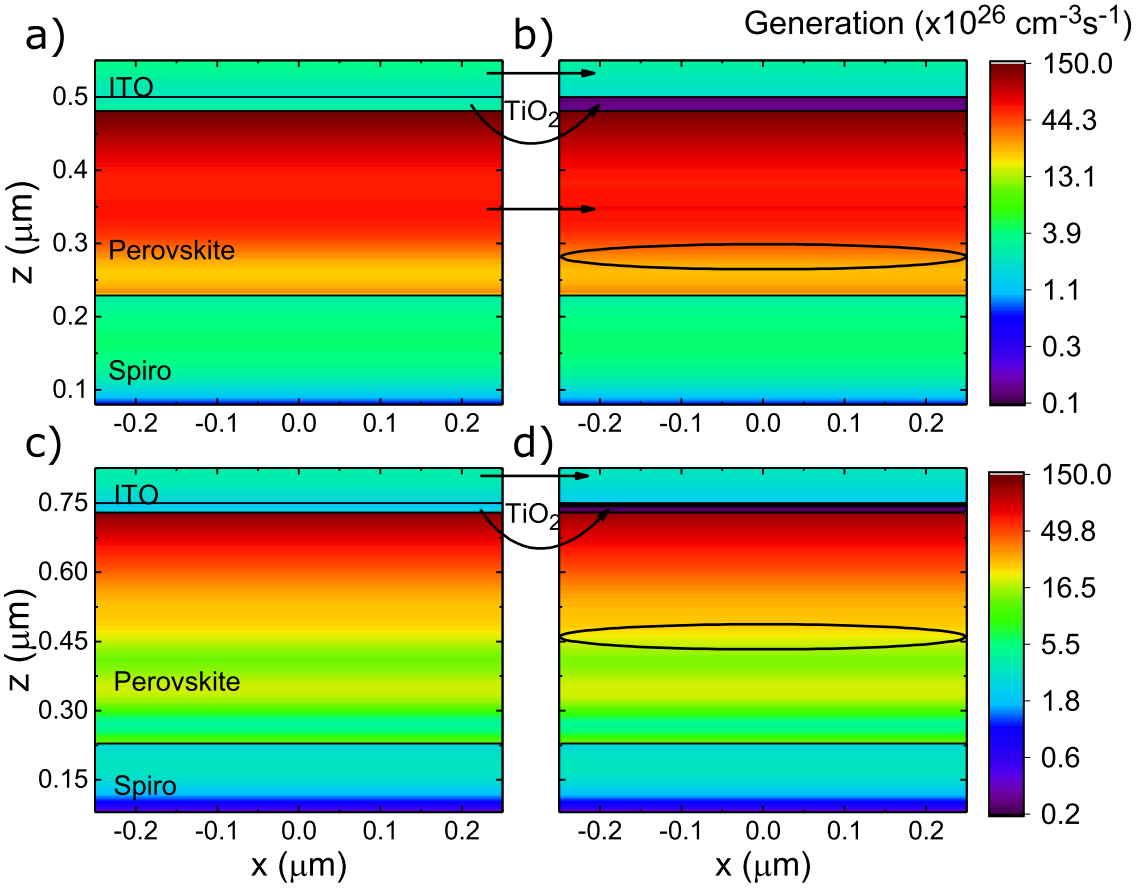

Figure 3.8: Generation profiles for the PCs with PBI. a) cell with 250 nm perovskite; b) cell with 250 nm perovskite and optimized spectrum; c) cell with 500 nm perovskite; d) cell with 500 nm perovskite and optimized spectrum. The arrows and ellipse mark the biggest changes in the plots.

the absorption due to the high intensity electric fields generated [72].

For this method, the format of the structures is rather important given that, according to the Fresnel's equations, the reflection increases for steeper refractive index changes. As a result, various studies were conducted, where different structures were tested to assess which one had the best optical performance [71]. The material used for these structures was TiO_2, because of its low parasitic absorption for wavelengths above 400 nm and its high dielectric constant (around 2.5) [70]. The use of this material in silicon solar cells does not result in any significant photocurrent losses as, in TiO_2 photoactive zone, silicon has a low absorption so TiO_2's parasitic absorption does not impact the cell performance. However, when considering perovskite, the degrading effects of TiO_2's photoactivity should be taken into account. As such, part of this section is centered in the effects of using an LDS material to minimize the absorption in the TiO_2 layer, that, in practice, should result in a lower degradation of the perovskite material.

3.4.1 Reflection Profiles

In Figure 3.9 are shown the plots for the simulated reflection of both PC with PBI, and LTC for 250 nm and 500 nm perovskite layers. Contrary to the PCs, this reflection is composed of a specular and a diffuse part due to the photonic structures envolved.

For the low wavelengths part of the spectrum, there is no significant change in the reflection, due to the good index matching between the background and ITO layer. It should be noted that, under 350 nm, a spike in reflection occurs, related with an increase in ITO's refractive index that reaches values up to 2.4 [80]. This spike is somewhat mitigated by employing photonic structures as they provide a better matching between the background and ITO.

The focal point to take into account here is the lower reflection for higher wavelengths, stemming from the use of photonic structures. It should be noted that the dips occurring above 800 nm, evidenced in the reflection profiles, arise from localized modes that are created inside the absorber material leading to a significant increase in the cell absorption. These modes are observed and discussed in the following section.

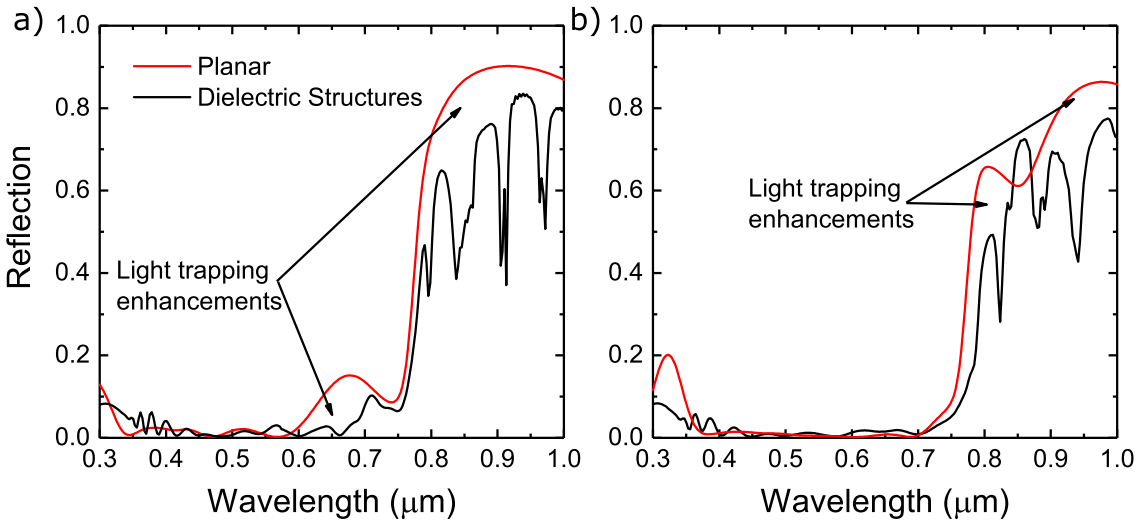

Figure 3.9: a) Reflection profile for the LTC, in black; and for the PC, in red; where both have a 250 nm layer of perovskite absorber material. b) Reflection profile for the LTC, in black; and for the PC, in red; where both have a 500 nm perovskite absorber material.

3.4.2 Absorption Profiles

Similarly to the last section, the next step consists in the calculation of the absorption profiles due to their important relation with the photocurrent parameter, used to characterize the optical performance of the cell. Again, the $A = 1 - R$ relation is seen. In Figure 3.10 are shown the absorption profiles obtained for LTC with the absorption of the perovskite absorber, TiO_2 and remaining materials distinguished by color. Inset are also shown 2 contour plots of the absorbed power density for 350 nm, bottom graph and 900 nm, top graph.

At a first glance, comparing with the previous PC results (Figure 3.4), one immediately notices the significant increase in TiO_2's absorption. Previously, for wavelengths ranging from 300 nm to 400 nm, results were around 10-20%, while, in this case, they rose to values between 60-80%, representing a shading of the absorber material for this wavelengths range. The main reason leading to this change is the thicker TiO_2 layer used, as predicted by the Beer-Lambert law. Considering the absorbed power density plots for 350 nm, one can also see this effect, since TiO_2 represents the majority of absorbed power by the cell. Consequently, one will expect that the effect of changing the incident spectrum will lead to an overall increase in the photocurrent generated by the cell.

An increased absorption of low energy photons is observed, reminiscent of the localized modes created inside the absorber material, consequence of the photonic structures employed. An example of these modes can be seen in the 900 nm wavelengths inset plots (top plots) in Figure 3.10, deriving from the different interferences generated by the interaction of light with the structures, consequently leading to the significant increase of the cell absorption.

Comparing the absorption of the remaining materials, namely ITO and Spiro, shown by the green shaded zone in the plots, with their equivalent absorption for the PCs. For wavelengths between 400 and 700 nm the absorption increases minimally from 1-3% to 3-4%. Under 400 nm this absorption went from 10-20% to 20-30%. While, above 700 nm it increased from 4-5% to 8-10%. These overall trends are related with the structures employed, as the increased surface area to improve the index matching between the background and the cell, also leads to higher overall parasitic absorption.

3.4.3 Photocurrent Shifts

Analogous to the PCs, sweeps were performed, where the λ_C and $\Delta\lambda$, for the LDS materials, were varied between 300 nm to 400 nm and 100 nm to 400 nm, respectively, to emulate the shifted spectrum as described in Figure 3.1. The results are shown in Figure 3.11 and the optimized values, along with their corresponding $\Delta\lambda$ and λ_C, are summarized in Table 3.3 and 3.4, respectively.

The main aspect resulting from these plots, when compared to the PCs, is the higher increase in J_{ph} when the DS spectrum is applied. The PCs saw increases shy of 1% while, in this case, the increase was ~2%. This improvement is linked to the higher TiO_2 absorption, associated with the increased thickness, as evidenced by the absorption plots from Figure 3.4, for the PC, and Figure 3.10, for the LTC. While a 2% increase may seem as small, it should be noted that, the maximum gain attainable, by absorbing the entire AM1.5G spectrum for wavelengths between 300 nm and 400 nm, is 1.35 mA/cm^2 (value calculated from the integration of the solar flux for the indicated range). Considering the different absorption plots shown throughout this work, the outstanding perovskite absorption under 700 nm is one of its most eye-catching features. As such, and understandably, introducing LDS as a manner to significantly increase J_{ph}, ends up falling short

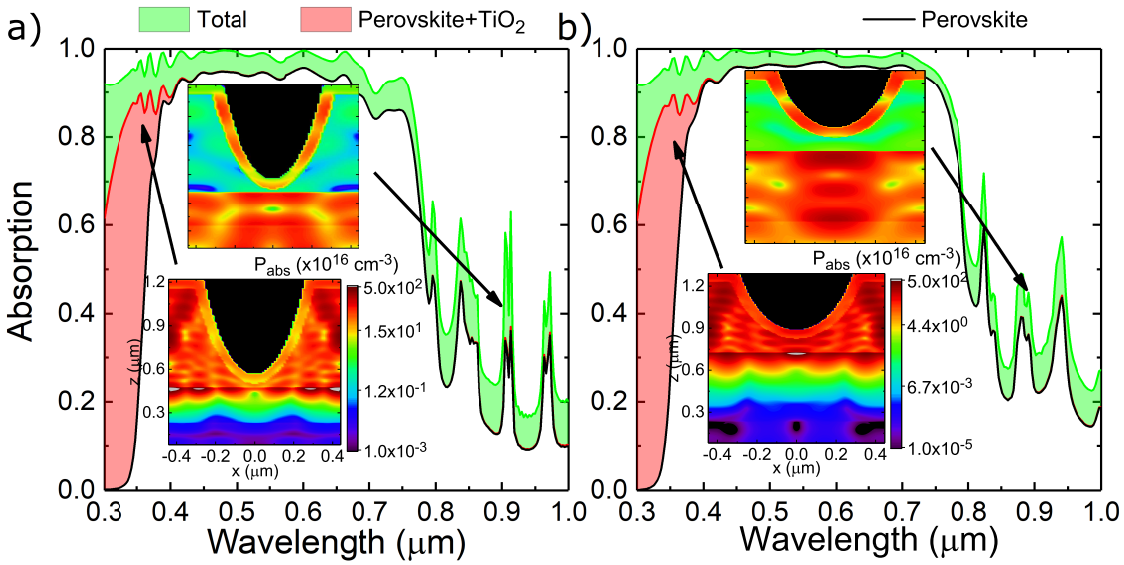

Figure 3.10: a) Absorption profile for the LTC with 250 nm perovskite layer, b) absorption profiles for the LTC with 500 nm perovskite layer. The shaded areas represent the absorption of the TiO_2, in red; and the remaining materials absorption, in green. The black curve is the perovskite absorption. The inset plots represent the absorbed power density for each respective cell for a wavelength of 350 nm, bottom graph, and 900 nm, top graph.

on major performance improvements, even when considering the ideal case here used for the shifting process. It should be noted that, the main objective of this method is to avoid the stability hindering TiO_2 photo-generation and harmful perovskite UV absorption without negatively impacting these cell's optical performance. Furthermore, given the optical nature of these studies, electrical phenomenon such as recombination are not considered which, in their own terms, can also benefit from lower UV radiation and higher visible radiation [53].

Table 3.3: Optimized J_{ph} results of the λ_C and $\Delta\lambda$ sweep done. It's shown the pristine results, AM1.5G J_{ph}; the results corresponding to the maximum value obtained from the sweep, J_{ph}; and the absolute and relative difference between both values ΔJ_{ph}.

Perovskite thickness (nm)	250	500
AM1.5G J_{ph} (mA/cm^2)	26.09	28.07
Shifted J_{ph} (mA/cm^2)	26.66	28.62
ΔJ_{ph} (mA/cm^2)	0.57	0.55
ΔJ_{ph} (%)	2.2	2.0

Similarly, to the PC, for higher $\Delta\lambda$ and λ_C, the cell's optical current suffers a steep decrease. Taking the example of the 250 nm cell (Figure 3.11 b)), the pristine value, shown in the plots by a thicker line, is 26.09 mA/cm^2. For a $\Delta\lambda$ and λ_C of 400 nm a J_{ph} value under 24.3 mA/cm^2 is observed, representing a decrease of almost 7%. Consequently,

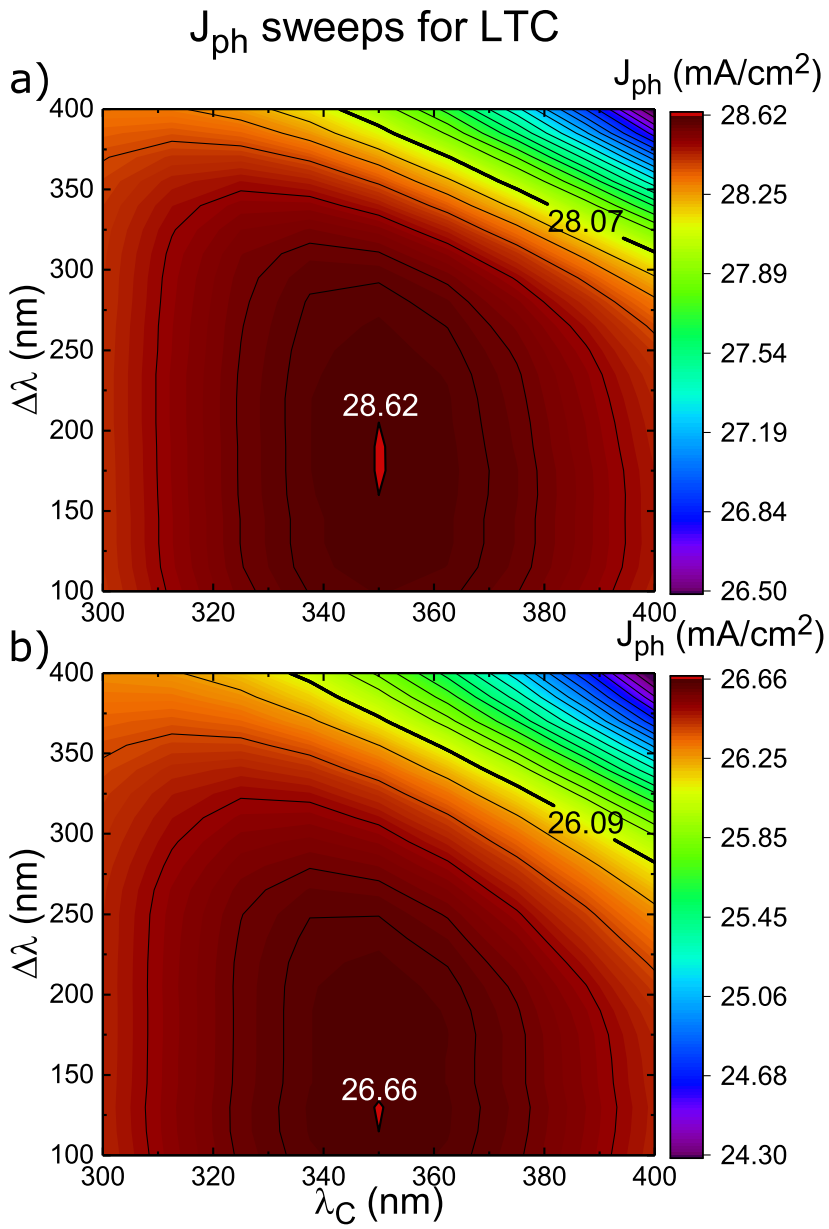

Figure 3.11: Contour plots for the sweeps where λ_C and $\Delta\lambda$ were changed from 300 nm to 400 nm and 100 nm to 400 nm, respectively. a) Plot for the cell with 250 nm perovskite layer and b) plot for the cell with 500 nm perovskite layer. The thicker line represents the contour corresponding to the photocurrent value obtained for the pristine spectrum. The indicated values represent the respective contour photocurrent value. The topmost value refers to the contour representing the pristine value, while the bottommost refers to the highest value contour in the plot.

the use of suboptimal shifting and absorption properties of DS materials can significantly hinder the cell performance, as evidenced by the redshifting (Figure 3.1 a)) to wavelengths where the cell shows worse absorption (Figure 3.10).

Considering the optimal $\Delta\lambda$ and λ_C values. One can see that the λ_C leading to improved optical performance is 350 nm for both cases, which resembles the behavior previously verified for the PCs with PBI. This result is expected, as these photonic structures mainly affect the absorption for higher wavelength photons, that are not significantly affected by LDS particles. On the other hand, $\Delta\lambda$ tends to fluctuate between each case. For these cells, $\Delta\lambda$ changes from 130 nm for the 250 nm cell to 190 nm for the 500 nm cell. However, when considering the photocurrent shift plots, the difference is mainly irrelevant as it represents changes under 0.1%. One should also note that the maximum photocurrent is obtained when the spectrum is shifted to around 500 nm, which is of particular importance, as electrically, the external quantum efficiency measured for these cells tends to have a maximum near this point [13, 52, 53, 61].

Table 3.4: $\Delta\lambda$ and λ_C, values corresponding to the optimum J_{ph} values. The values on the left represent the thickness of the perovskite used in the cell simulation.

Perovskite thickness (nm)	λ_C **(nm)**	$\Delta\lambda$ **(nm)**
250	350	130
500	350	190

3.4.4 Generation Profiles

This study was finalized by calculating the generation profile for the LTC, whose plots are shown in Figure 3.12. The left plots represent the pristine generation profiles, while the right plots represent the generation with the optimized spectrum discussed in the last subsection. The most notable aspect is the significant reduction in the TiO_2 photo-generation with the spectral change. For the 250 nm cell, in the evidenced part of the plot, the photo-generation decreased from 0.42×10^{26} to 0.03×10^{26} mA/cm^2. The 500 nm cell, suffered a similar decrease from 0.16×10^{26} mA/cm^2 to 0.03×10^{26} mA/cm^2, representing reductions of one order of magnitude in the harmful TiO_2 photo-generation. These results are equivalent to those of the PC, although in this case the higher TiO_2 thickness helps understand the reduction better.

As pointed out in the generation profiles of Figure 3.12, a small decrease in the generation peak, located in the perovskite's top corners, is observed. This reduction is a consequence of the UV spectrum redshift, where light has a higher penetration depth and, therefore, instead of highly concentrated absorption near the absorber material top interface, there is a more delocalized absorption throughout the absorber volume. This effect can be electrically favorable for the cell as there is less surface absorption and, consequently, less recombination.

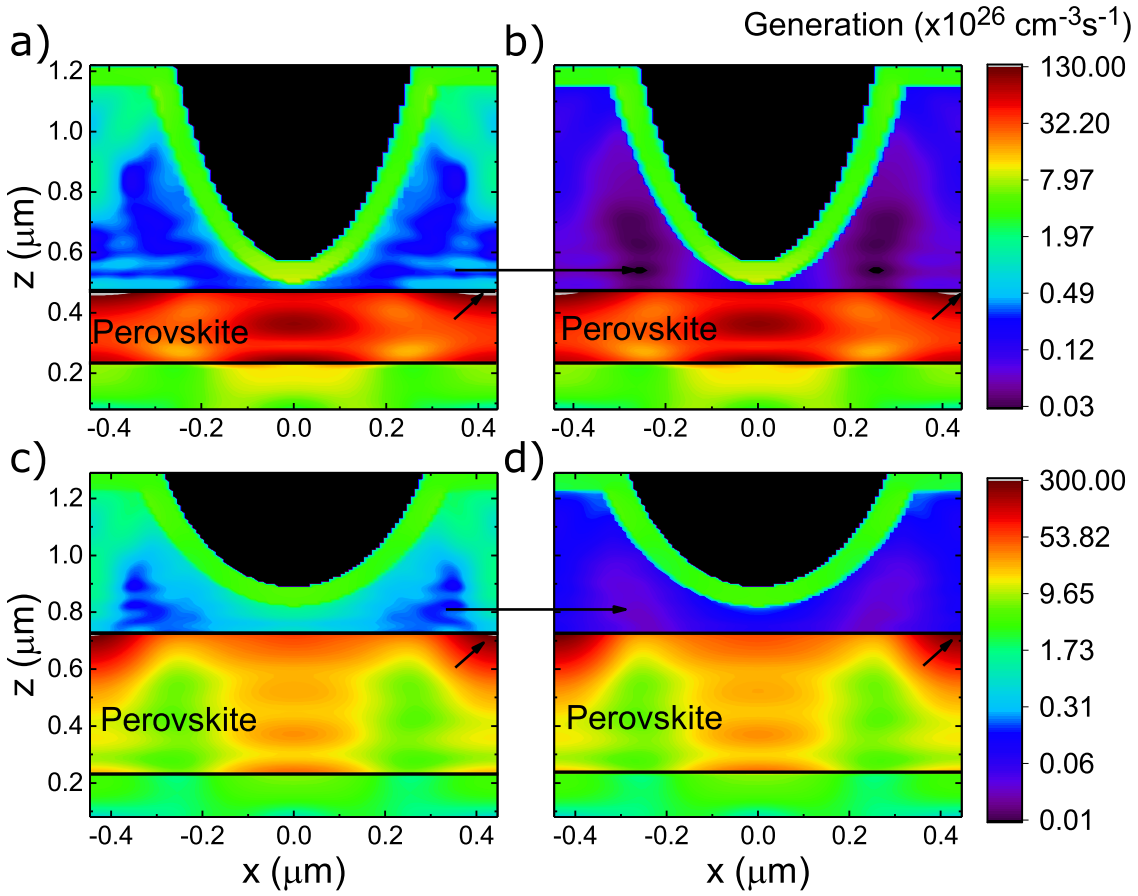

Figure 3.12: Generation profiles for the LTC. a) cell with 250 nm perovskite; b) cell with 250 nm perovskite and optimized spectrum; c) cell with 500 nm perovskite; d) cell with 500 nm perovskite and optimized spectrum. The arrows point to the biggest plot changes.

Similar to Subsection 3.3.4, an evaluation of the perovskite's UV absorption was made by calculating J_{ph} for these different cases. The values obtained for the LTC with 250 nm perovskite were 0.68 mA/cm^2 and 0.13 mA/cm^2 for the pristine and optimized spectra, respectively, while the LTC with 500 nm perovskite saw a reduction from 0.73 mA/cm^2 to 0.13 mA/cm^2. The above-mentioned values represent reductions ~80%, which is very similar to those of the previously studied PCs. Therefore, an important decrease in perovskite's UV absorption was obtained. Granted, the simulation methodology here employed does not attend to all intricacies of the DS process, however, these results demonstrate some interesting general results coming from the adoption of these materials on PSCs that could improve the device's life-span. In fact, recent studies from different research groups, have used LDS materials on PSC's to achieve a better life-span [60–62]. One example, by Anizelli et. al., even compared the results against a UV filter obtaining equivalent long-term values for the cell parameters [52].

3.5 Final Thoughts

To summarize the fundamental results from this work, a bar chart was made, where the J_{ph} improvements and UV absorption reductions are shown (Figure 3.13).

Starting with the photocurrent chart (Figure 3.13 a)). A first point to be made is the higher current for the 500 nm cells, resulting from the thicker absorber. This difference is reminiscent of higher VIS-NIR radiation absorption, as demonstrated in Figure 3.4 for the PC and Figure 3.10 for the LTC. Secondly, the higher for the PBI PC, when compared with VBI PC, that stems from better index matching between the background and the first material in the cell (ITO), as seen in Figure 3.4. The 500 nm cell, for the PBI case, can even come close to the LTC with 250 nm. However, it should be noted that the dimensions here used for the LTC were based on optimizations done for a VBI case. Consequently, the VIS-NIR absorption improvements are not as high as they should be in its optimized application.

A last analysis of this graph also indicates small current increases when using the optimized spectrum. Considering these studies were made without any losses, Figure 3.1 a), it can be inferred that these materials do not show a pronounced increase in optical performance. However, electrical effects, that were not considered in this work, like bulk instead of surface absorption and lower thermal losses that come with higher energy transitions, can be deciding factors leading to improved cell current.

Considering now the bar chart analyzing the UV J_{ph}. As referred in earlier sections, this parameter is indicative of the overall cell absorption for the selected range. Consequently, by calculating this value between 300 nm and 400 nm, one can assess the UV absorption of these cells. From the chart, a reduction around 80% is observed for all cases. This constitutes a major reduction in the perovskite's absorption, even when one considers the idealized DS case here employed. Therefore, by maintaining a similar optical current, while significantly reducing the harmful effects of UV radiation in these cells, one would expect an increased long-term performance.

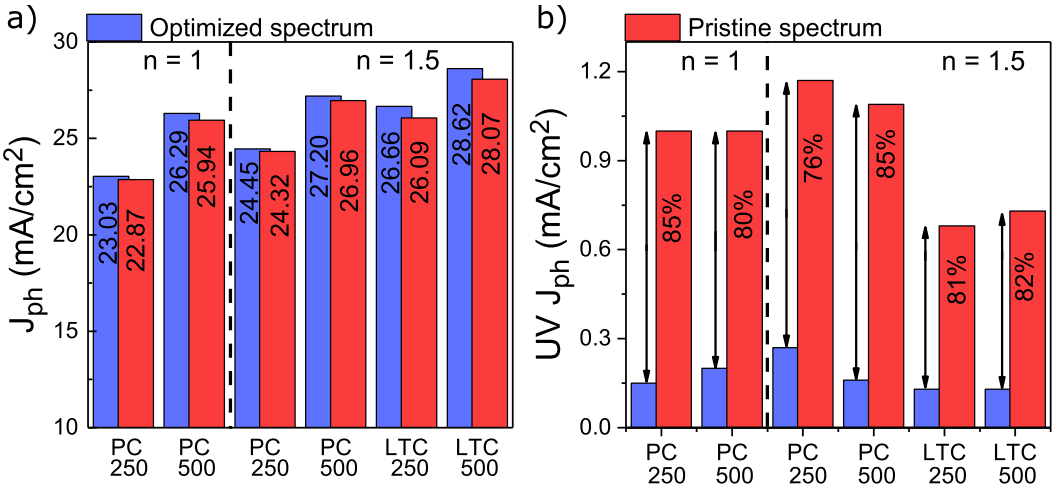

Figure 3.13: a) Bar chart summarizing the pristine (red) and optimized (blue) J_{ph} values obtained from the photocurrent sweeps; b) Bar chart summarizing the J_{ph} for wavelengths ranging from 300 nm to 400 nm for the for the pristine (red) and optimized spectrum (blue).

Chapter 4

Conclusion and Future Perspectives

A theoretical study on the viability of applying LDS particles to reduce PSC's UV degradation was made. The findings here discussed are in accordance with those experimentally accomplished in recent literature.

The use of these materials did not reveal a pronounced increase in photocurrent, as was seen by the photocurrent sweeps done (subsections 3.3.3 and 3.4.3). Here, the maximum change is ~2% for the cells with photonic structures and 1% for the planar cells, with the main difference being attributed to the lower TiO_2 thickness of the latter. On the other hand, the use of unoptimized $\Delta\lambda$ and λ_C can severely impact the optical performance of the cell, reducing the photocurrent by 7%, for the worst cases simulated. The optimum $\Delta\lambda$ and λ_C implied a spectrum shift to wavelengths around 500 nm, blending well with the PSC's electrical performance peak.

Importantly, from the performed analysis related with perovskite stability, one obtained a significant reduction in TiO_2 harmful photo-generation of one order of magnitude, coupled with an increase in perovskite bulk generation (Figure 3.7, 3.8 and 3.12). By assessing the perovskite UV photocurrent for the different simulated cells, reductions ~80% were obtained when comparing J_{ph} values for the pristine and changed spectrum (subsection 3.3.4 and 3.4.4). Therefore, from these analyses, one can infer that the use of LDS avoids the unwanted effects of UV radiation on the perovskite, demonstrated by the hefty decrease in UV absorption coupled with the diminished TiO_2 photoactivity resulting from lower photo-generation.

This work establishes a generalized optical analysis of using luminescent down-shifting materials to reduce TiO_2 generation and perovskite's UV absorption. Here, optimized light trapping structures for a vacuum index background were used, while the employed background was 1.5 to accommodate an encapsulation with luminescent down-shifting materials. Therefore, an optimization, following this work, for a 1.5 background index

case is expected. Furthermore, a study on the uncertanty propagation on the FDTD method should also be done for improved analysis when comparing different photocurrent values.

Following this work, one also expects that further studies will be centered in the different luminescent down-shifting materials to assess which are the most beneficial for photocurrent gains and long-term performance of these cells, guided by the results attained here. Although there's already several studies where these materials are used to achieve the previously mentioned gains, there is still no study, at least to the author's knowledge, where all LDS materials are compared to each other. Therefore, by knowing the ones that offer best performance, one can optimize their benefits and, consequently, they can then be used as a helping factor in overcoming the major problems that still plague perovskite-based photovoltaic technology.

References

[1] International Energy Agency. *Snapshot of global photovoltaic markets*. 2017.

[2] S. Philipps and W. Warmuth. ©*Fraunhofer ISE: Photovoltaics Report*. 2018.

[3] SolarPower Europe. *Global market outlook for Solar Power 2017-2021*. 2017.

[4] SolarPower Europe. *Global market outlook for Solar Power/2016-2020*. 2016.

[5] M. A. Green. "Commercial progress and challenges for photovoltaics." In: *Nature Energy* 1.1 (2016), p. 15015. DOI: 10.1038/nenergy.2015.15.

[6] D. Keszler and J. Wager. *Novel Materials Development for Polycrystalline Thin-Film Solar Cells*. Tech. rep. 2008.

[7] R. Kotipalli, O. Poncelet, G. Li, Y. Zeng, L. Francis, B. Vermang, and D. Flandre. "Addressing the impact of rear surface passivation mechanisms on ultra-thin Cu(In,Ga)Se_2 solar cell performances using SCAPS 1-D model." In: *Solar Energy* 157.August (2017), pp. 603–613. ISSN: 0038092X. DOI: 10.1016/j.solener.2017.08.055.

[8] P. M. P. Salomé, B. Vermang, R. Ribeiro-Andrade, J. P. Teixeira, J. M. V. Cunha, M. J. Mendes, S. Haque, J. Borme, H. Águas, E. Fortunato, R. Martins, J. C. González, J. P. Leitão, P. A. Fernandes, M. Edoff, and S. Sadewasser. "Passivation of Interfaces in Thin Film Solar Cells: Understanding the Effects of a Nanostructured Rear Point Contact Layer." In: *Advanced Materials Interfaces* 5.2 (2018), p. 1701101. ISSN: 21967350. DOI: 10.1002/admi.201701101.

[9] H.-W. Schock and R. Noufi. "CIGS-based solar cells for the next millennium." In: *Progress in Photovoltaics: Research and Applications* 8.1 (2000), pp. 151–160. ISSN: 1062-7995. DOI: 10.1002/(SICI)1099-159X(200001/02)8:1<151::AID-PIP302>3.0.CO;2-Q.

[10] A. Kojima, K. Teshima, Y. Shirai, and T. Miyasaka. "Organometal Halide Perovskites as Visible-Light Sensitizers for Photovoltaic Cells." In: *Journal of the American Chemical Society* 131.17 (2009), pp. 6050–6051. DOI: 10.1021/ja809598r.

[11] N. J. Jeon, J. H. Noh, W. S. Yang, Y. C. Kim, S. Ryu, J. Seo, and S. I. Seok. "Compositional engineering of perovskite materials for high-performance solar cells." In: *Nature* 517.7535 (2015), pp. 476–480. DOI: 10.1038/nature14133.

[12] F. Giordano, A. Abate, J. P. Correa Baena, M. Saliba, T. Matsui, S. H. Im, S. M. Zakeeruddin, M. K. Nazeeruddin, A. Hagfeldt, and M. Graetzel. "Enhanced electronic properties in mesoporous TiO_2 via lithium doping for high-efficiency perovskite solar cells." In: *Nature Communications* 7 (2016), p. 10379. DOI: 10.1038/ncomms10379.

[13] F. Fu, T. Feurer, T. P. Weiss, S. Pisoni, E. Avancini, C. Andres, S. Buecheler, and A. N. Tiwari. "High-efficiency inverted semi-transparent planar perovskite solar cells in substrate configuration." In: *Nature Energy* 2.1 (2016), p. 16190. DOI: 10.1038/nenergy.2016.190.

[14] W. S. Yang, J. H. Noh, N. J. Jeon, Y. C. Kim, S. Ryu, J. Seo, and S. I. Seok. "High-performance photovoltaic perovskite layers fabricated through intramolecular exchange." In: *Science* 348.6240 (2015), pp. 1234–1237. DOI: 10.1126/science.aaa9272.

[15] J.-P. Correa-Baena, M. Saliba, T. Buonassisi, M. Grätzel, A. Abate, W. Tress, and A. Hagfeldt. "Promises and challenges of perovskite solar cells." In: *Science* 358.6364 (2017), pp. 739–744. DOI: 10.1126/science.aam6323.

[16] *National Energy Renewable Laboratory (NREL)*. URL: https://www.nrel.gov/.

[17] M. Asghar, J. Zhang, H. Wang, and P. Lund. "Device stability of perovskite solar cells – A review." In: *Renewable and Sustainable Energy Reviews* 77.May (2017), pp. 131–146. DOI: 10.1016/j.rser.2017.04.003.

[18] T. M. Brenner, D. A. Egger, L. Kronik, G. Hodes, and D. Cahen. "Hybrid organic—inorganic perovskites: low-cost semiconductors with intriguing charge-transport properties." In: *Nature Reviews Materials* 1.1 (2016), p. 15007. DOI: 10.1038/natrevmats.2015.7.

[19] N. J. Jeon, H. G. Lee, Y. C. Kim, J. Seo, J. H. Noh, J. Lee, and S. I. Seok. "o -Methoxy Substituents in Spiro-OMeTAD for Efficient Inorganic–Organic Hybrid Perovskite Solar Cells." In: *Journal of the American Chemical Society* 136.22 (2014), pp. 7837–7840. DOI: 10.1021/ja502824c.

[20] C. L. Davies, M. R. Filip, J. B. Patel, T. W. Crothers, C. Verdi, A. D. Wright, R. L. Milot, F. Giustino, M. B. Johnston, and L. M. Herz. "Bimolecular recombination in methylammonium lead triiodide perovskite is an inverse absorption process." In: *Nature Communications* 9.1 (2018), p. 293. DOI: 10.1038/s41467-017-02670-2.

[21] J. H. Noh, S. H. Im, J. H. Heo, T. N. Mandal, and S. I. Seok. "Chemical Management for Colorful, Efficient, and Stable Inorganic–Organic Hybrid Nanostructured Solar Cells." In: *Nano Letters* 13.4 (2013), pp. 1764–1769. DOI: 10.1021/nl400349b.

[22] M. R. Filip, C. Verdi, and F. Giustino. "GW Band Structures and Carrier Effective Masses of CH 3 NH 3 PbI 3 and Hypothetical Perovskites of the Type $APbI_3$:A = NH_4, PH_4, AsH_4 ,and SbH_4." In: *The Journal of Physical Chemistry C* 119.45 (2015), pp. 25209–25219. DOI: 10.1021/acs.jpcc.5b07891.

[23] E. Mosconi, P. Umari, and F. De Angelis. "Electronic and optical properties of mixed Sn–Pb organohalide perovskites: a first principles investigation." In: *Journal of Materials Chemistry A* 3.17 (2015), pp. 9208–9215. DOI: 10.1039/C4TA06230B.

[24] W.-J. Yin, J.-H. Yang, J. Kang, Y. Yan, and S.-H. Wei. "Halide perovskite materials for solar cells: a theoretical review." In: *Journal of Materials Chemistry A* 3.17 (2015), pp. 8926–8942. DOI: 10.1039/C4TA05033A.

[25] A. Martí and G. L. Araújo. "Limiting efficiencies for photovoltaic energy conversion in multigap systems." In: *Solar Energy Materials and Solar Cells* 43.2 (1996), pp. 203–222. DOI: 10.1016/0927-0248(96)00015-3.

[26] W. Shockley and H. J. Queisser. "Detailed Balance Limit of Efficiency of p-n Junction Solar Cells." In: *Journal of Applied Physics* 32.3 (1961), pp. 510–519. DOI: 10.1063/1.1736034.

[27] A. De Vos. "Detailed balance limit of the efficiency of p-n junction solar cells." In: *Journal of Physics D: Applied Physics* 13.83946 (1980), pp. 839–846.

[28] J. E. Parrott. "The limiting efficiency of an edge-illuminated multigap solar cell." In: *Journal of Physics D: Applied Physics* 12.3 (1979), pp. 441–450. DOI: 10.1088/0022-3727/12/3/014.

[29] H Pauwels and A De Vos. "Determination of the maximum efficiency solar cell structure." In: *Solid-State Electronics* 24.9 (1981), pp. 835–843. DOI: 10.1016/0038-1101(81)90099-X.

[30] U. Mehmood, A. Al-Ahmed, M. Afzaal, F. A. Al-Sulaiman, and M. Daud. "Recent progress and remaining challenges in organometallic halides based perovskite solar cells." In: *Renewable and Sustainable Energy Reviews* 78.May (2017), pp. 1–14. DOI: 10.1016/j.rser.2017.04.105.

[31] A. Djurisic, F. Liu, H. Tam, M. Wong, A. Ng, C. Surya, W. Chen, and Z. He. "Perovskite solar cells - An overview of critical issues." In: *Progress in Quantum Electronics* 53.June (2017), pp. 1–37. DOI: 10.1016/j.pquantelec.2017.05.002.

[32] H. Shen, T. Duong, J. Peng, D. Jacobs, N. Wu, J. Gong, Y. Wu, S. K. Karuturi, X. Fu, K. Weber, X. Xiao, T. P. White, and K. Catchpole. "Mechanically-stacked perovskite/CIGS tandem solar cells with efficiency of 23.9% and reduced oxygen sensitivity." In: *Energy & Environmental Science* 11.2 (2018), pp. 394–406. DOI: 10.1039/C7EE02627G.

[33] M. Jaysankar, M. Filipic, B. Zielinski, R. Schmager, W. Song, W. Qiu, U. W. Paetzold, T. Aernouts, M. Debucquoy, R. Gehlhaar, and J. Poortmans. "Perovskite–silicon tandem solar modules with optimised light harvesting." In: *Energy & Environmental Science* 11.6 (2018), pp. 1489–1498. DOI: 10.1039/C8EE00237A.

[34] K. A. Bush, A. F. Palmstrom, Z. J. Yu, M. Boccard, R. Cheacharoen, J. P. Mailoa, D. P. McMeekin, R. L. Z. Hoye, C. D. Bailie, T. Leijtens, I. M. Peters, M. C. Minichetti, N. Rolston, R. Prasanna, S. Sofia, D. Harwood, W. Ma, F. Moghadam, H. J. Snaith, T. Buonassisi, Z. C. Holman, S. F. Bent, and M. D. McGehee. "23.6%-efficient monolithic perovskite/silicon tandem solar cells with improved stability." In: *Nature Energy* 2.4 (2017), p. 17009. DOI: 10.1038/nenergy.2017.9.

[35] E. Klampaftis, D. Ross, K. R. McIntosh, and B. S. Richards. "Enhancing the performance of solar cells via luminescent down-shifting of the incident spectrum: A review." In: *Solar Energy Materials and Solar Cells* 93.8 (2009), pp. 1182–1194. DOI: 10.1016/j.solmat.2009.02.020.

[36] N. Liu, H. Xue, Y. Ji, and J. Wang. "ZnSe/ZnS core-shell quantum dots incorporated with Ag nanoparticles as luminescent down-shifting layers to enhance the efficiency of Si solar cells." In: *Journal of Alloys and Compounds* 747 (2018), pp. 696–702. DOI: 10.1016/j.jallcom.2018.03.060.

[37] R. Rondão, A. R. Frias, S. F. H. Correia, L. Fu, V. de Zea Bermudez, P. S. André, R. A. S. Ferreira, and L. D. Carlos. "High-Performance Near-Infrared Luminescent Solar Concentrators." In: *ACS Applied Materials & Interfaces* 9.14 (2017), pp. 12540–12546. DOI: 10.1021/acsami.7b02700.

[38] K. R. McIntosh, G. Lau, J. N. Cotsell, K. Hanton, D. L. Bätzner, F. Bettiol, and B. S. Richards. "Increase in external quantum efficiency of encapsulated silicon solar cells from a luminescent down-shifting layer." In: *Progress in Photovoltaics: Research and Applications* 17.3 (2009), pp. 191–197. DOI: 10.1002/pip.867.

[39] B. Lipovšek, A. Solodovnyk, K. Forberich, E. Stern, J. Krč, C. J. Brabec, and M. Topič. "Optical model for simulation and optimization of luminescent down-shifting layers filled with phosphor particles for photovoltaics." In: *Optics Express* 23.15 (2015), A882. DOI: 10.1364/OE.23.00A882.

[40] R. Lesyuk, V. Lesnyak, A. Herguth, D. Popovych, Y. Bobitski, C. Klinke, and N. Gaponik. "Simulation study of environmentally friendly quantum-dot-based photovoltaic windows." In: *Journal of Materials Chemistry C* 5.45 (2017), pp. 11790–11797. DOI: 10.1039/C7TC02945D.

[41] R. Lesyuk, V. Marinov, E. K. Hobbie, A. Elbaradei, I. Tarnavchyk, and Y. Bobitski. "Toward cadmium-free spectral down-shifting converters for photovoltaic applications." In: *Solar Energy Materials and Solar Cells* 151 (2016), pp. 52–59. DOI: 10.1016/j.solmat.2016.02.021.

[42] A. J. Chatten, K. W. J. Barnham, B. F. Buxton, and M. A. Malik. "Quantum Dot Solar Concentrators." In: *Semiconductors* 38.8 (2004), pp. 949–957.

[43] A. Chatten, K. Barnham, B. Buxton, N. Ekins-Daukes, and M. Malik. "A new approach to modelling quantum dot concentrators." In: *Solar Energy Materials and Solar Cells* 75.3-4 (2003), pp. 363–371. DOI: 10.1016/S0927-0248(02)00182-4.

[44] S. F. Correia, P. P. Lima, P. S. André, M. R. S. Ferreira, and L. A. D. Carlos. "High-efficiency luminescent solar concentrators for flexible waveguiding photovoltaics." In: *Solar Energy Materials and Solar Cells* 138 (2015), pp. 51–57. DOI: 10.1016/j.solmat.2015.02.032.

[45] S. F. Correia, P. P. Lima, E. Pecorato, S. J. Ribeiro, P. S. André, R. A. Ferreira, and L. D. Carlos. "Scale up the collection rea of luminescent solar concentrators towards metre-length flexible waveguiding photovoltaics." In: *Progress in Photovoltaics: Research and Applications* 24 (2016), pp. 1178–1193. DOI: 10.1002/pip.

[46] J. Wiegman and E. van der Kolk. "Building integrated thin film luminescent solar concentrators: Detailed efficiency characterization and light transport modelling." In: *Solar Energy Materials and Solar Cells* 103 (2012), pp. 41–47. DOI: 10.1016/j.solmat.2012.04.016.

[47] W. G. van Sark, K. W. Barnham, L. H. Slooff, A. J. Chatten, A. Büchtemann, A. Meyer, S. J. McCormack, R. Koole, D. J. Farrell, R. Bose, E. E. Bende, A. R. Burgers, T. Budel, J. Quilitz, M. Kennedy, T. Meyer, C. D. M. Donegá, A. Meijerink, and D. Vanmaekelbergh. "Luminescent Solar Concentrators - A review of recent results." In: *Optics Express* 16.26 (2008), p. 21773. DOI: 10.1364/OE.16.021773.

[48] J. S. Batchelder, A. H. Zewai, and T. Cole. "Luminescent solar concentrators 1: Theory of operation and techniques for performance evaluation." In: *Applied Optics* 18.18 (1979), p. 3090. DOI: 10.1364/AO.18.003090.

[49] A. Hermann. "Luminescent solar concentrators - A review." In: *Solar Energy* 29.4 (1982), pp. 323–329.

[50] B. Rowan, L. Wilson, and B. Richards. "Advanced Material Concepts for Luminescent Solar Concentrators." In: *IEEE Journal of Selected Topics in Quantum Electronics* 14.5 (2008), pp. 1312–1322. DOI: 10.1109/JSTQE.2008.920282.

[51] J. Kettle, N. Bristow, D. Gethin, Z. Tehrani, O. Moudam, B. Li, E. Katz, G. dos Reis Benatto, and F. Krebs. "Printable luminescent down shifter for enhancing efficiency and stability of organic photovoltaics." In: *Solar Energy Materials and Solar Cells* 144 (2016), pp. 481–487. DOI: 10.1016/j.solmat.2015.09.037.

[52] H. S. Anizelli, V. Stoichkov, R. V. Fernandes, J. L. Duarte, E. Laureto, J. Kettle, I. Visoly-Fisher, and E. A. Katz. "Application of luminescence downshifting materials for enhanced stability of $CH_3NH_3PbI_{3_{(1-x)}}Cl_{3x}$ perovskite photovoltaic devices." In: *Organic Electronics* 49 (2017), pp. 129–134. DOI: 10.1016/j.orgel.2017.06.056.

[53] N. Chander, A. F. Khan, P. S. Chandrasekhar, E. Thouti, S. K. Swami, V. Dutta, and V. K. Komarala. "Reduced ultraviolet light induced degradation and enhanced light harvesting using YVO_4:Eu^{3+} down-shifting nano-phosphor layer in organometal halide perovskite solar cells." In: *Applied Physics Letters* 105.3 (2014), p. 033904. DOI: 10.1063/1.4891181.

[54] J Llanos, I Brito, D Espinoza, R. Sekar, and P. Manidurai. "A down-shifting Eu^{3+}-doped Y_2WO_6/TiO_2 photoelectrode for improved light harvesting in dye-sensitized solar cells." In: *Royal Society Open Science* 5.2 (2018), p. 171054. DOI: 10.1098/rsos.171054.

[55] W.-A. Quitsch, D. W. DeQuilettes, O. Pfingsten, A. Schmitz, S. Ognjanovic, S. Jariwala, S. Koch, M. Winterer, D. S. Ginger, and G. Bacher. "The Role of Excitation Energy in Photobrightening and Photodegradation of Halide Perovskite Thin Films." In: *The Journal of Physical Chemistry Letters* 9.8 (2018), pp. 2062–2069. DOI: 10.1021/acs.jpclett.8b00212.

[56] T. Leijtens, G. E. Eperon, S. Pathak, A. Abate, M. M. Lee, and H. J. Snaith. "Overcoming ultraviolet light instability of sensitized TiO_2 with meso-superstructured organometal tri-halide perovskite solar cells." In: *Nature Communications* 4.1 (2013), p. 2885. ISSN: 2041-1723. DOI: 10.1038/ncomms3885.

[57] S. Ito, S. Tanaka, K. Manabe, and H. Nishino. "Effects of Surface Blocking Layer of Sb_2S_3 on Nanocrystalline TiO_2 for $CH_3NH_3PbI_3$ Perovskite Solar Cells." In: *The Journal of Physical Chemistry C* 118.30 (2014), pp. 16995–17000. DOI: 10.1021/jp500449z.

[58] S.-W. Lee, S. Kim, S. Bae, K. Cho, T. Chung, L. E. Mundt, S. Lee, S. Park, H. Park, M. C. Schubert, S. W. Glunz, Y. Ko, Y. Jun, Y. Kang, H.-S. Lee, and D. Kim. "UV Degradation and Recovery of Perovskite Solar Cells." In: *Scientific Reports* 6.1 (2016), p. 38150. DOI: 10.1038/srep38150.

[59] A. Farooq, I. M. Hossain, S. Moghadamzadeh, J. A. Schwenzer, T. Abzieher, B. S. Richards, E. Klampaftis, and U. W. Paetzold. "Spectral Dependence of Degradation under Ultraviolet Light in Perovskite Solar Cells." In: *ACS Applied Materials & Interfaces* 10.26 (2018), pp. 21985–21990. DOI: 10.1021/acsami.8b03024.

[60] A. Gheno, T. Trigaud, J. Bouclé, P. Audebert, B. Ratier, and S. Vedraine. "Stability assessments on luminescent down-shifting molecules for UV-protection of perovskite solar cells." In: *Optical Materials* 75 (2018), pp. 781–786. DOI: 10.1016/j.optmat.2017.11.027.

[61] X. Hou, T. Xuan, H. Sun, X. Chen, H. Li, and L. Pan. "High-performance perovskite solar cells by incorporating a $ZnGa_2O_4$:Eu^{3+} nanophosphor in the mesoporous TiO_2 layer." In: *Solar Energy Materials and Solar Cells* 149 (2016), pp. 121–127. DOI: 10.1016/j.solmat.2016.01.021.

[62] B. Wang, B. Li, T. Shen, M. Li, and J. Tian. "ZnSe quantum dots downshifting layer for perovskite solar cells." In: *Journal of Energy Chemistry* 27.3 (2018), pp. 736–741. DOI: 10.1016/j.jechem.2017.11.021.

[63] T. Uekert, A. Solodovnyk, S. Ponomarenko, A. Osvet, I. Levchuk, J. Gast, M. Batentschuk, K. Forberich, E. Stern, H.-J. Egelhaaf, and C. J. Brabec. "Nanostructured organosilicon luminophores in highly efficient luminescent down-shifting layers for thin film photovoltaics." In: *Solar Energy Materials and Solar Cells* 155 (2016), pp. 1–8. DOI: 10.1016/j.solmat.2016.04.019.

[64] G. Yin, P. Manley, and M. Schmid. "Light trapping in ultrathin $CuIn_{1-x}Ga_xSe_2$ solar cells by dielectric nanoparticles." In: *Solar Energy* 163.January (2018), pp. 443–452. DOI: 10.1016/j.solener.2018.01.096.

[65] J. Bhattacharya, N. Chakravarty, S. Pattnaik, W. Dennis Slafer, R. Biswas, and V. L. Dalal. "A photonic-plasmonic structure for enhancing light absorption in thin film solar cells." In: *Applied Physics Letters* 99.13 (2011), p. 131114. DOI: 10.1063/1.3641469.

[66] D. G. Baranov, D. A. Zuev, S. I. Lepeshov, O. V. Kotov, A. E. Krasnok, A. B. Evlyukhin, and B. N. Chichkov. "All-dielectric nanophotonics: the quest for better materials and fabrication techniques." In: *Optica* 4.7 (2017), p. 814. DOI: 10.1364/OPTICA.4.000814.

[67] O. Isabella, R. Vismara, D. Linssen, K. Wang, S. Fan, and M. Zeman. "Advanced light trapping scheme in decoupled front and rear textured thin-film silicon solar cells." In: *Solar Energy* 162.October 2017 (2018), pp. 344–356. DOI: 10.1016/j.solener.2018.01.040.

[68] J. Xiao, H. Fang, R. Su, K. Li, J. Song, T. F. Krauss, J. Li, and E. R. Martins. "Paths to light trapping in thin film GaAs solar cells." In: *Optics Express* 26.6 (2018), A341. DOI: 10.1364/OE.26.00A341.

[69] Y. J. Donie, M. Smeets, A. Egel, F. Lentz, J. B. Preinfalk, A. Mertens, V. Smirnov, U. Lemmer, K. Bittkau, and G. Gomard. "Light trapping in thin film silicon solar cells via phase separated disordered nanopillars." In: *Nanoscale* 10.14 (2018), pp. 6651–6659. DOI: 10.1039/C8NR00455B.

[70] M. J. Mendes, A. Araújo, A. Vicente, H. Águas, I. Ferreira, E. Fortunato, and R. Martins. "Design of optimized wave-optical spheroidal nanostructures for photonic-enhanced solar cells." In: *Nano Energy* 26 (2016), pp. 286–296. DOI: 10.1016/j.nanoen.2016.05.038.

[71] M. J. Mendes, S. Haque, O. Sanchez-Sobrado, A. Araújo, H. Águas, E. Fortunato, and R. Martins. "Optimal-Enhanced Solar Cell Ultra-thinning with Broadband Nanophotonic Light Capture." In: *iScience* 3 (2018), pp. 238–254. DOI: 10.1016/j.isci.2018.04.018.

[72] M. L. Brongersma, Y. Cui, and S. Fan. "Light management for photovoltaics using high-index nanostructures." In: *Nature Materials* 13.5 (2014), pp. 451–460. DOI: 10.1038/nmat3921.

[73] O. Sanchez-Sobrado, M. J. Mendes, S. Haque, T. Mateus, A. Araujo, H. Aguas, E. Fortunato, and R. Martins. "Colloidal-lithographed TiO_2 photonic nanostructures for solar cell light trapping." In: *Journal of Materials Chemistry C* 5.27 (2017), pp. 6852–6861. DOI: 10.1039/C7TC01756A.

[74] J. Grandidier, M. G. Deceglie, D. M. Callahan, and H. A. Atwater. "Simulations of solar cell absorption enhancement using resonant modes of a nanosphere array." In: *Physics, Simulation, and Photonic Engineering of Photovoltaic Devides*. Ed. by A. Freundlich and J.-F. F. Guillemoles. Vol. 8256. 2012, p. 825603. DOI: 10.1117/12.909677.

[75] M. G. Deceglie, V. E. Ferry, A. P. Alivisatos, and H. A. Atwater. "Design of Nanostructured Solar Cells Using Coupled Optical and Electrical Modeling." In: *Nano Letters* 12.6 (2012), pp. 2894–2900. DOI: 10.1021/nl300483y.

[76] S. D. Gedney. *Introduction to the Finite-Difference Time-Domain(FDTD) Method for Electromagnetics*. 2011, p. 236. ISBN: 9781608455225.

[77] *Lumerical Inc.* URL: http://www.lumerical.com/tcad-products/fdtd/.

[78] Kane Yee. "Numerical solution of initial boundary value problems involving maxwell's equations in isotropic media." In: *IEEE Trans. Antennas Propag.* 14.3 (1966), pp. 302–307. DOI: 10.1109/TAP.1966.1138693.

[79] A. T. Vicente, A. Araújo, M. J. Mendes, D. Nunes, M. J. Oliveira, O. Sanchez-Sobrado, M. P. Ferreira, H. Águas, E. Fortunato, and R. Martins. "Multifunctional cellulose-paper for light harvesting and smart sensing applications." In: *Journal of Materials Chemistry C* 6.13 (2018), pp. 3143–3181. DOI: 10.1039/C7TC05271E.

[80] M. N. Polyanskiy. *Refractive index database*. URL: https://refractiveindex.info.

[81] F. Purcell-Milton and Y. K. Gun'ko. "Quantum dots for Luminescent Solar Concentrators." In: *Journal of Materials Chemistry* 22.33 (2012), p. 16687. DOI: 10.1039/c2jm32366d.

[82] B. Richards and K. McIntosh. "Overcoming the poor short wavelength spectral response of CdS/CdTe photovoltaic modules via luminescence down-shifting: ray-tracing simulations." In: *Progress in Photovoltaics: Research and Applications* 15.1 (2007), pp. 27–34. DOI: 10.1002/pip.723.

ANNEX I

Equations for the FDTD method

In Chapter 1, one example equation was used to show the effect of applying the central differences to the Maxwell's equations, namely, for the z component projection of Faraday's law. Consequently, here are shown the remaining equations resulting from the application of the central difference to the other components of Faradays's law, Equation I.1 and I.2 for the x and y component, respectively.

$$\mu\left(\frac{H^{n+1}_{x_{i,j+\frac{1}{2},k+\frac{1}{2}}} - H^{n}_{x_{i,j+\frac{1}{2},k+\frac{1}{2}}}}{\Delta t}\right) = \left(\frac{E^{n+\frac{1}{2}}_{y_{i,j+1,k+1}} - E^{n+\frac{1}{2}}_{y_{i,j+\frac{1}{2},k}}}{\Delta z}\right) - \left(\frac{E^{n+\frac{1}{2}}_{z_{i,j+1,k+\frac{1}{2}}} - E^{n+\frac{1}{2}}_{z_{i,j,k+\frac{1}{2}}}}{\Delta y}\right) - M^{n+\frac{1}{2}}_{x_{i,j+\frac{1}{2},k+\frac{1}{2}}} \tag{I.1}$$

$$\mu\left(\frac{H^{n+1}_{y_{i+\frac{1}{2},j,k+\frac{1}{2}}} - H^{n}_{y_{i+\frac{1}{2},j,k+\frac{1}{2}}}}{\Delta t}\right) = \left(\frac{E^{n+\frac{1}{2}}_{z_{i+1,j,k+\frac{1}{2}}} - E^{n+\frac{1}{2}}_{z_{i,j,k+\frac{1}{2}}}}{\Delta x}\right) - \left(\frac{E^{n+\frac{1}{2}}_{x_{i+\frac{1}{2},j,k+1}} - E^{n+\frac{1}{2}}_{x_{i+\frac{1}{2},j,k}}}{\Delta z}\right) - M^{n+\frac{1}{2}}_{y_{i+\frac{1}{2},j,k+\frac{1}{2}}} \tag{I.2}$$

The next step consists in calculating equivalent equations for the Ampere's law. Equation I.3 shows the x-projection of Ampere's law, when central difference is applied.

$$\epsilon\left(\frac{E^{n+\frac{1}{2}}_{x_{i+\frac{1}{2},j,k}} - E^{n}_{x_{i+\frac{1}{2},j,k}}}{\Delta t}\right) = \left(\frac{H^{n}_{z_{i+\frac{1}{2},j+\frac{1}{2},k}} - H^{n}_{z_{i+\frac{1}{2},j-\frac{1}{2},k}}}{\Delta y}\right) - \left(\frac{H^{n}_{y_{i+\frac{1}{2},j,k+\frac{1}{2}}} - H^{n}_{y_{i+\frac{1}{2},j,k-\frac{1}{2}}}}{\Delta z}\right) - J^{n}_{x_{i+\frac{1}{2},j,k}} \tag{I.3}$$

As a result, the discrete forms of both Ampere and Faraday's law, when combined, lead to six different equations (Equation I.4 to Equation I.9) that can be used, together with some initial parameters, to create an iterative process to solve electromagnetic problems by calculating the evolution of the electric and magnetic fields through time. These equations establish the foundation for the application of the FDTD method.

$$H^{n+1}_{x_{i,j+\frac{1}{2},k+\frac{1}{2}}} =$$

$$H^{n}_{x_{i,j+\frac{1}{2},k+\frac{1}{2}}} + \frac{\Delta t}{\mu}\left[\left(\frac{E^{n+\frac{1}{2}}_{y_{i,j+\frac{1}{2},k+1}} - E^{n+\frac{1}{2}}_{y_{i,j+\frac{1}{2},k}}}{\Delta z}\right) - \left(\frac{E^{n+\frac{1}{2}}_{z_{i,j+1,k+\frac{1}{2}}} - E^{n+\frac{1}{2}}_{z_{i,j+1,k+\frac{1}{2}}}}{\Delta y}\right) - M^{n+\frac{1}{2}}_{x_{i,j+\frac{1}{2},k+\frac{1}{2}}}\right] \tag{I.4}$$

$$H^{n+1}_{y_{i+\frac{1}{2},j,k+\frac{1}{2}}} =$$

$$H^{n}_{y_{i+\frac{1}{2},j,k+\frac{1}{2}}} + \frac{\Delta t}{\mu}\left[\left(\frac{E^{n+\frac{1}{2}}_{z_{i+1,j,k+\frac{1}{2}}} - E^{n+\frac{1}{2}}_{z_{i,j,k+\frac{1}{2}}}}{\Delta x}\right) - \left(\frac{E^{n+\frac{1}{2}}_{x_{i+\frac{1}{2},j,k+1}} - E^{n+\frac{1}{2}}_{x_{i+\frac{1}{2},j,k}}}{\Delta z}\right) - M^{n+\frac{1}{2}}_{y_{i+\frac{1}{2},j,k}}\right] \tag{I.5}$$

$$H^{n+1}_{z_{i+\frac{1}{2},j+\frac{1}{2},k}} =$$

$$H^{n}_{z_{i+\frac{1}{2},j+\frac{1}{2},k}} + \frac{\Delta t}{\mu}\left[\left(\frac{E^{n+\frac{1}{2}}_{x_{i+\frac{1}{2},j+1,k}} - E^{n+\frac{1}{2}}_{x_{i+\frac{1}{2},j,k}}}{\Delta y}\right) - \left(\frac{E^{n+\frac{1}{2}}_{y_{i+1,j+\frac{1}{2},k}} - E^{n+\frac{1}{2}}_{y_{i,j+\frac{1}{2},k}}}{\Delta x}\right) - M^{n+\frac{1}{2}}_{z_{i+\frac{1}{2},j+\frac{1}{2},k}}\right] \tag{I.6}$$

$$E^{n+\frac{1}{2}}_{x_{i+\frac{1}{2},j,k}} =$$

$$E^{n-\frac{1}{2}}_{x_{i+\frac{1}{2},j,k}} + \frac{\Delta t}{\epsilon}\left[\left(\frac{H^{n}_{x_{i+\frac{1}{2},j+\frac{1}{2},k}} - H^{n}_{z_{i+\frac{1}{2},j-\frac{1}{2},k}}}{\Delta y}\right) - \left(\frac{H^{n}_{y_{i+\frac{1}{2},j,k+\frac{1}{2}}} - H^{n}_{y_{i+\frac{1}{2},j,k-\frac{1}{2}}}}{\Delta z}\right) - J^{n}_{x_{i+\frac{1}{2},j,k}}\right] \tag{I.7}$$

$$E^{n+\frac{1}{2}}_{y_{i,j+\frac{1}{2},k}} =$$

$$E^{n-\frac{1}{2}}_{y_{i,j+\frac{1}{2},k}} + \frac{\Delta t}{\epsilon}\left[\left(\frac{H^{n}_{x_{i,j+\frac{1}{2},k+\frac{1}{2}}} - H^{n}_{x_{i,j+\frac{1}{2},k-\frac{1}{2}}}}{\Delta z}\right) - \left(\frac{H^{n}_{z_{i+\frac{1}{2},j+\frac{1}{2},k}} - H^{n}_{z_{i-\frac{1}{2},j+\frac{1}{2},k}}}{\Delta x}\right) - J^{n}_{y_{i,j+\frac{1}{2},k}}\right] \tag{I.8}$$

$$E^{n+\frac{1}{2}}_{z_{i,j,k+\frac{1}{2}}} =$$

$$E^{n-\frac{1}{2}}_{z_{i,j,k+\frac{1}{2}}} + \frac{\Delta t}{\epsilon}\left[\left(\frac{H^{n}_{y_{i+\frac{1}{2},j,k+\frac{1}{2}}} - H^{n}_{y_{i-\frac{1}{2},j,k+\frac{1}{2}}}}{\Delta x}\right) - \left(\frac{H^{n}_{x_{i,j+\frac{1}{2},k+\frac{1}{2}}} - H^{n}_{x_{i,j-\frac{1}{2},k+\frac{1}{2}}}}{\Delta x}\right) - J^{n}_{z_{i,j,k+\frac{1}{2}}}\right] \tag{I.9}$$

ANNEX II

Simulation Parameters

In this annex is provided the material data, in specific the refractive index, n, and the extinction coefficient, k, used for the simulations shown in this work, Figure II.1. The most important simulation parameters used for these simulations are also summarized in Table II.1.

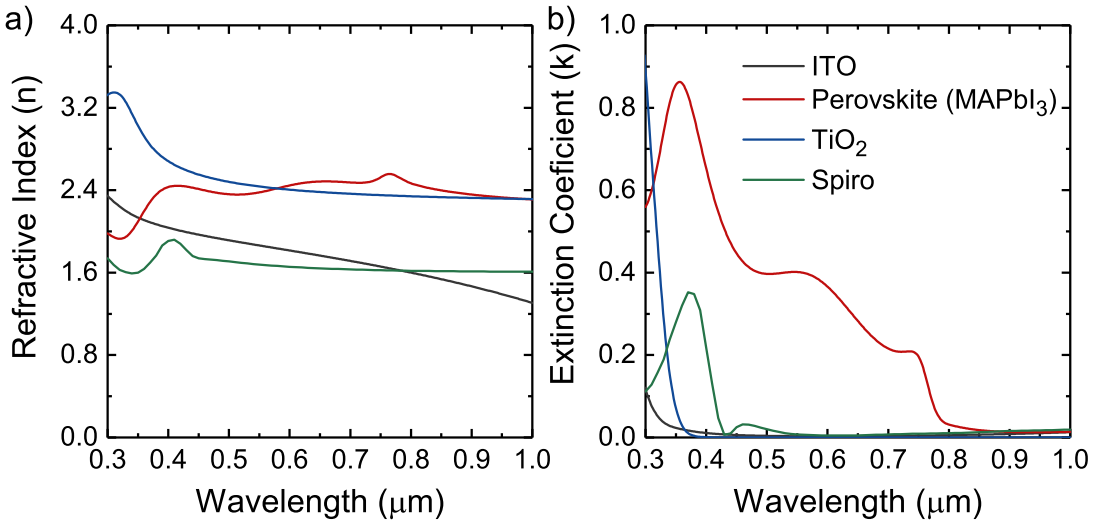

Figure II.1: Refractive index, n, and extinction coeficient, k, for the different material used in the simulations. These values are provided by reference [80].

Table II.1: Most important simulation parameters used, namely the different boundary conditions for the various cells, the PML layers and the background mesh used. The PC with PBI and VBI had the same simulation parameters.

		Boundary Conditions				PML	Mesh**
		z_{max}	z_{min}	x*	y*	layers	
Planar	250 nm	PML	PML	Anti-Symmetric	Anti-Symmetric	32	5
	500 nm	PML	PML	Anti-Symmetric	Anti-Symmetric	32	5
Photonic structures	250 nm	PML	PML	Anti-Symmetric	Anti-Symmetric	36	3
	500 nm	PML	PML	Anti-Symmetric	Anti-Symmetric	36	3

* These conditions are equivalent to having periodic boundary conditions.
** This mesh refers to the background of simulation, however mesh overrides were also employed to help reduce the computational costs of these simulations.

ANNEX III

Simulated Transmissions

Figure III.1 shows both the theoretical and simulated transmission for the planar cells with vacuum background, Figure III.2 shows the same results for the planar cells with a background index of 1.5 and Figure III.3 shows the simulated transmission for the cells with photonics structures. Firstly, it should be highlighted that the obtained transmissions ~0 were expected, due to the metallic back contact used in the simulated solar cells. For the first two graphs, the variation between the theoretical and simulated results derives from the iterative process used for the simulations. Because these transmission values are so low, they are more prone to be affected by simulation errors that come from using a numerical simulation method. However, one can still see that the FDTD simulation results perform an admirable fit to the theoretical results.

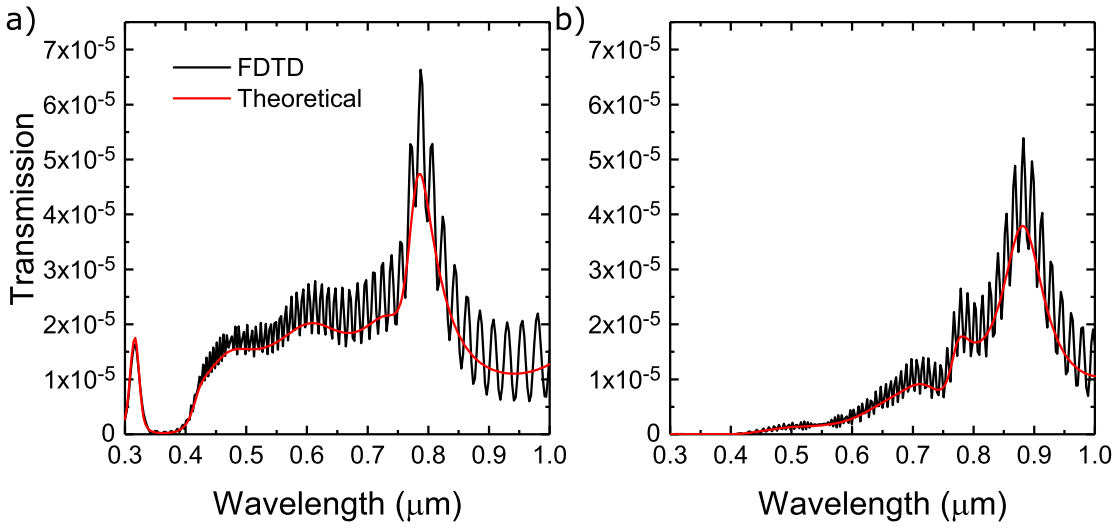

Figure III.1: Simulated and theoretical transmission for the planar cells. a) 250 nm perovskite and b) 500 nm perovskite.

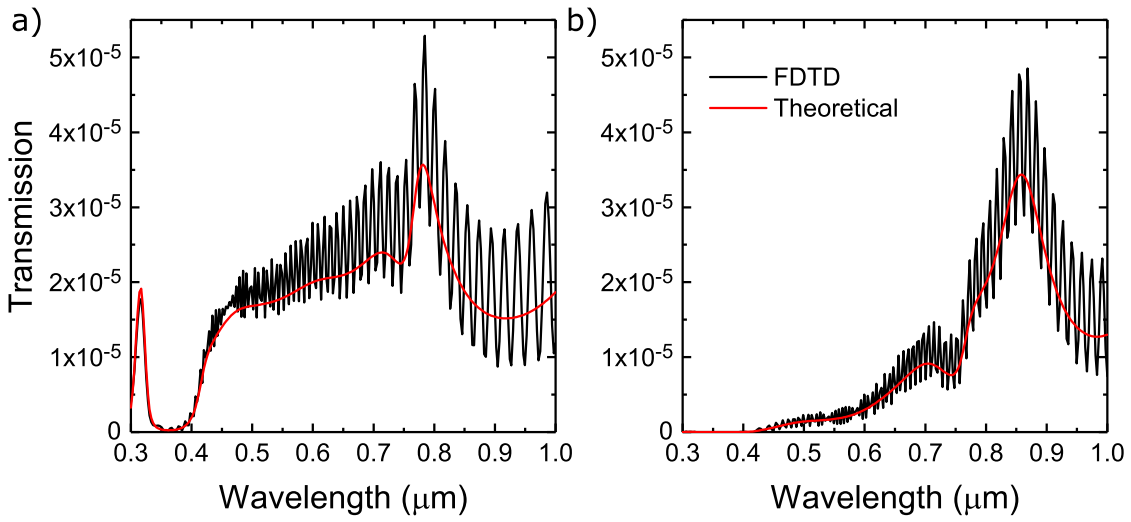

Figure III.2: Simulated and theoretical transmission for the planar cells with a background index of 1.5. a) 250 nm perovskite and b) 500 nm perovskite.

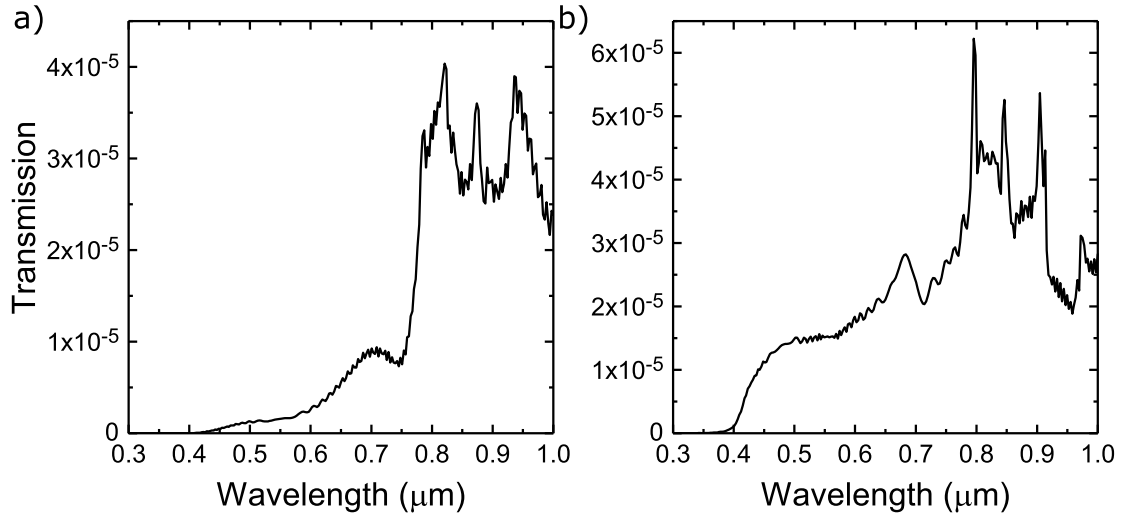

Figure III.3: Simulated transmission for the cells with photonic structures and a background index of 1.5. a) 500 nm perovskite and b) 250 nm perovskite.